Mechanics of Materials 173 (2022) 104432

Contents lists available at ScienceDirect

Mechanics of Materials

journal homepage: www.elsevier.com/locate/mecmat

Mechanically-grown morphogenesis of Voronoi-type materials: Computer design, 3D-printing and experiments

Z. Hooshmand-Ahoor [a], M.G. Tarantino [b], K. Danas [a,*]

[a] LMS, C.N.R.S., École Polytechnique, Institut Polytechnique de Paris, 91128 Palaiseau, France
[b] ICMMO/SP2M, C.N.R.S., Université Paris-Saclay, 91405 Orsay, France

ARTICLE INFO

Keywords:
Voronoi materials
Porous materials
Architected materials
Computational morphogenesis
Void growth
3D-printing

ABSTRACT

The present work introduces a novel and versatile computer-design and experimental strategy to obtain random Voronoi-type geometries, called M-Voronoi (from mechanically grown), with smooth void shapes and variable intervoid ligament sizes that can reach very low relative densities. This is achieved via a numerical, large strain, nonlinear elastic, void growth mechanical process. Originally small circular voids embedded in a cell of arbitrary shape (triangle, circle, rectangle, trapezoid) grow when subjected to displacement (Dirichlet) boundary conditions. The deformed voids evolve into smooth Voronoi-type geometrical shapes leading to macroscopic isotropy or anisotropy depending on the prescribed boundary conditions. The void growth process is a direct consequence of mass conservation and the incompressibility of the surrounding nonlinear elastic matrix phase and the final achieved relative density may be analytically estimated in terms of the determinant of the applied deformation gradient. In order to study the mechanical properties of the M-Voronoi materials, we focus on two-dimensional porous polymer square representative isotropic and anisotropic geometries in terms of void size and realization, which are 3D-printed and experimentally tested under uniaxial compression. For comparison, we also test random polydisperse porous materials with circular voids, standard eroded Voronoi geometries and hexagonal honeycombs. The first two are also isotropic while the latter are only isotropic in the linear elastic regime. We show that the randomness of the M-Voronoi geometry and their non-uniform intervoid ligament size leads to enhanced mechanical properties at large compressive strains with no apparent peak-stress and strong hardening well before densification. By comparing them with the hexagonal geometries, which tend to exhibit a peak-stress and a plateau-type response, we show that the hardening response of the M-Voronoi is mainly due to their geometrical characteristics and less due to the polymer hardening response. Anisotropic M-Voronoi are also produced and tested indicating that anisotropy only enhances the initial stiffness along the longitudinal direction but instead leads to lower buckling loads and hardening rates than the corresponding isotropic M-Voronoi in the nonlinear regime.

1. Introduction

Numerous living organisms, from plants to animals, possess a distinctive internal architecture that evolves during ontogeny. Morphological evolution in natural systems underpins a variety of life functions, including growth, locomotion and predation. For example, plants transport water and other minerals through an intricate network of hollow channels, the *aerenchyma*, whose size and shape change during plant growth (Corson et al., 2009; Zhao et al., 2018). Likewise, skeletal muscles enable us to run and walk via the contraction of multiply innervated (randomly distributed) fibers whose surrounding connective tissue, the *extracellular matrix*, thickens during motoneuron lesions (Tidball and Wehling-Henricks, 2004; Spyrou et al., 2019). These are only a few enticing examples that show the functional diversity enabled in living organisms by morphogenesis.

Unlike nature where morphogenesis occurs naturally via multiple actuation mechanisms (chemical, mechanical, electrical, thermal, etc.), synthetic systems require robust computational algorithms or man-made processing methods to evolve. Over the past two decades, significant efforts have been made to harness computational morphogenesis in synthetic structures. Examples are numerous and can be found in many areas of research including materials science (Portela et al., 2020; Tarantino et al., 2019; Zerhouni et al., 2019; Kumar et al., 2020), mechanobiology (Spyrou et al., 2019; Zhao et al., 2018; Ma et al., 2021), design (Martínez et al., 2016, 2018; Aage et al., 2017;

* Corresponding author.
E-mail addresses: zahra.hooshmand-ahoor@polytechnique.edu (Z. Hooshmand-Ahoor), gabriella.tarantino@universite-paris-saclay.fr (M.G. Tarantino), konstantinos.danas@polytechnique.edu (K. Danas).

https://doi.org/10.1016/j.mechmat.2022.104432
Received 9 May 2022; Received in revised form 29 June 2022; Accepted 7 August 2022
Available online 11 August 2022

Baandrup et al., 2020) and architecture (Menges, 2012; Roudavski, 2009). In particular, in the context of materials science and mechanics, today one is able to mimic complex heterogeneous structures that are reminiscent of bone (Portela et al., 2020; Kumar et al., 2020; Martínez et al., 2016, 2018; Aage et al., 2017; Wu et al., 2017), skeletal muscles (Spyrou et al., 2019), plants (Faisal et al., 2012; Zhao et al., 2018) and even particle-reinforced polymers (Segurado and Llorca, 2002; Lopez-Pamies et al., 2013) and geomaterials (Roberts and Teubner, 1995; Roberts and Garboczi, 2001). Traditionally, computational morphogenesis has relied on voxel-based algorithms that enable generating complex distributions of Voronoi polyhedra. The latter typically consist of beam elements with uniform thickness and variable length, which are arranged in a disordered manner to form either a 2D (Spyrou et al., 2019; Tekoglu et al., 2011) or a 3D structure (Martínez et al., 2016, 2018; Aage et al., 2017; Baandrup et al., 2020). In the context of additive manufacturing, Voronoi polyhedra generated by tessellation enable the design of multi-phase composite structures and can feature very low solid densities, if the inclusion phase is taken as void. On the other hand, tessellated Voronoi cellular materials contain points of high stress concentration thereby proving highly sensitive to geometrical and fabrication defects like many truss- and shell-based lattices (Ashby and Gibson, 1997; Onck et al., 2001; Papka and Kyriakides, 1994, 1998; Deshpande et al., 2001; Symons and Fleck, 2008; O'Masta et al., 2017; Liu et al., 2017; Bonatti and Mohr, 2019). They may thus be further optimized especially for use in applications where large nonlinear deformations, buckling loads and fractures are involved (e.g. energy, bending stiffness). To overcome this issue, in very recent years novel periodic plate-based cellular materials (see for instance Tancogne-Dejean et al., 2018; Wang and Sigmund, 2021) as well as non-periodic porous architectures have been designed, optimized and studied experimentally. Notable examples include double gyroid nanolattices (Crossland et al., 2008; Prusty et al., 2020) and microlattices (Maskery et al., 2017) very recently extended to stochastic geometries (Al-Ketan et al., 2021), as well as spinoidal Gaussian architectures using both threshold and phase-field methods (Teubner, 1991; Roberts and Teubner, 1995; Roberts and Garboczi, 2001; Hsieh et al., 2019; Khristenko et al., 2020) and machine-learning techniques (Kumar et al., 2020). Another random geometry is that of polydisperse (i.e. multiple size) particulate microstructures designed via a random adsorption algorithm (RSA) combined with computational homogenization (Torquato, 2002; Segurado and Llorca, 2002; Lopez-Pamies et al., 2013; Anoukou et al., 2018; Tarantino et al., 2019; Zerhouni et al., 2019). Of course a large class of low-density random porous solids involves foams (see for instance Deshpande and Fleck (2000) and Gong and Kyriakides (2005)). In the present study, we will include a two-dimensional equivalent of the foam geometry, that of standard Voronoi to be discussed later.

Specifically, solid model spinodal topologies can feature a density range between 0.7 and 0.2 (Maskery et al., 2017; Hsieh et al., 2019), whereas corresponding shell models can achieve ultra-low densities but usually lead to anisotropic response beyond the linear elastic response, while due to their perfect periodicity, they are susceptible to long wavelength instabilities and localization bands that span the entire specimen. In turn, Gaussian type topologies have only a limited range of mechanical responses and are known to be non-optimal (Roberts and Garboczi, 2001; Zerhouni et al., 2021) when compared with rigorous mathematical bounds in linear elasticity but can be versatile in obtaining isotropic and anisotropic responses by design (Kumar et al., 2020). By contrast, random polydisperse distributions of spherical voided inclusions dispersed into a dense matrix (Zerhouni et al., 2019; Tarantino et al., 2019) are mechanically nearly optimal in the linear regime as their moduli have been shown (both numerically and experimentally) to lie very close to the Hashin–Shtrikman bounds (Hashin and Shtrikman, 1963). Yet, they require an increasingly large smallest-to-largest void size ratio to reach low relative densities. This in turn leads to practical difficulties in realizing representative – especially in the nonlinear regime – material response that can be produced with high accuracy by current additive manufacturing technologies, both metallic and polymeric, as we will show in the present study.

More generally, most lightweight porous materials are great candidates for energy absorption and structural applications because of their particular compressive response which may be divided into three regimes: (i) an initial almost linear regime up to a peak-stress, (ii) a stress-oscillating plateau or very low hardening regime and finally (iii) a strongly hardening regime, called as densification. Without giving the most general discussion here for the sake of brevity, one may attribute the peak-stress and subsequent plateau to a combination of an elastic buckling instability and/or plastic localization or even secondary bifurcations (see for instance discussions in Ashby and Gibson (1997), Triantafyllidis and Schraad (1998) and Schaedler and Carter (2016)). In brittle polymers, fracture of ligaments occurs before or immediately after elastic instabilities following the peak-stress (Thornton and Magee, 1975; Ashby and Gibson, 1997; Triantafillou and Gibson, 1990; Bi et al., 2020). In turn, the recent study of Luan et al. (2022) has focused on the compressive response of flexible elastomers, where the effect of smoothness of the intervoid ligaments and polydispersity of void size has been addressed numerically. Therein, those two geometrical characteristics were shown to affect both the initial stiffness of foams (which is in qualitative agreement with the experimental work of Zerhouni et al. (2019)) as well as the level of the peak-stress.

1.1. Scope of the study

In this regard, the present work proposes a novel computational morphogenesis process allowing to design random (i.e., non-periodic) composite materials that contain *smooth, polydisperse* Voronoi-type inclusions with *non-uniform* intervoid ligament thicknesses randomly embedded into a base matrix phase. This process is developed drawing inspiration from prior studies on epithelial cell remodeling (Liu et al., 2010; Kasza et al., 2014) and is implemented using a finite-element (FE) framework. The response of the resulting geometries is studied experimentally using 3D-printing. Specifically, it consists in deforming numerically – under uniform displacement (Dirichlet) boundary conditions – an arbitrarily-shaped convex cell that contains a discrete number of circular void inclusions. The latter are randomly dispersed into a non-linear elastic matrix phase and are generated via the general-purpose RSA algorithm developed in Segurado and Llorca (2002) and Lopez-Pamies et al. (2013). Countless composites architectures can be generated with this process depending on the type of the inclusion phase, which may be void, solid or fluid-like and can potentially span relative densities from zero to unity. For illustrative purposes, this study will focus on two-dimensional porous inclusions embedded in a semi-brittle polymer solid. We will then thoroughly investigate experimentally the mechanical response of the porous architectures at various relative densities. The new void geometries resemble closely the polyhedra obtained by standard Voronoi tessellations but differ in two ways; they comprise non-uniform intervoid ligament thickness and have smooth void boundaries. Due to the mechanically-grown origin of the void geometry, we call these materials M-Voronoi throughout the study. We note that the heart of the process, which is based on a numerical nonlinear elastic energy minimization and uniform displacement boundary conditions, is independent of dimension and shape of the primary cell (provided it is convex). The latter allows the seamless assembly of the individual cells (of any porosity) in macro-geometries of any shape and variable spatial stiffness. We will show in particular that the M-Voronoi exhibit continuous strong hardening (and thus no apparent peak-stress) well before densification.

This paper is organized as follows. In Section 2, the numerical construction process of the M-Voronoi geometry is presented. Various representative numerical realizations of the porous topologies obtained by this method are presented and compared with other existing random porous geometries. The experimental methods including

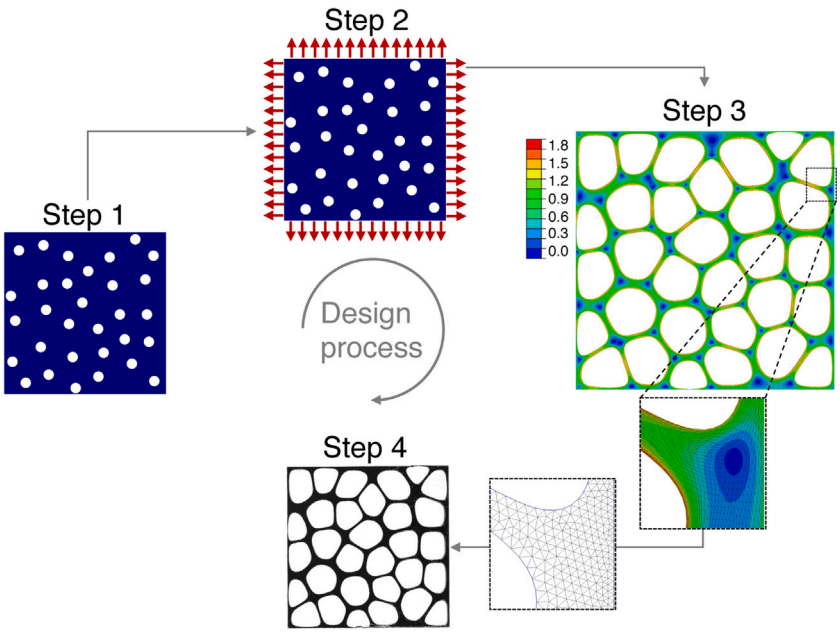

Fig. 1. Computational process for the generation of the M-Voronoi material. For illustration purposes, the diagram shows the five steps required to obtain a virtual M-Voronoi geometry starting from a square unit cell containing a discrete number of mono-sized circular pores. Step 1: Random distribution of circular holes in a square domain. Step 2: Application of uniform displacement boundary conditions. Step 3: Numerical FE simulation at large strains using nonlinear elastic energy minimization and incompressible matrix behavior. The zoom image shows locally the deformed mesh. The color bar indicates the maximum principal logarithmic strain. Step 4: Uniform re-scaling of the deformed geometry to the desired size. Remeshing (as shown in the zoomed image), 3D extrusion and STL generation of the final geometry used for 3D-printing. (For interpretation of the references to color in this figure legend, the reader is referred to the web version of this article.)

the 3D-printing strategy and the protocol for the mechanical tests are described in Section 3. In Section 4, we show experimental uniaxial compression results corresponding to the aforementioned geometries. First, we analyze the representativity of the M-Voronoi response in terms of different realizations and the size of voids. Subsequently, we compare first the M-Voronoi with two additional random porous geometries. The first comprises random distributions of circular voids of various sizes (i.e. polydisperse), termed as RSA from the random adsorption algorithm (Lopez-Pamies et al., 2013; Anoukou et al., 2018), and the second is obtained by a recently proposed uniformly eroded Voronoi tessellation algorithm, named E-Voronoi, that has been used to model muscles (Spyrou et al., 2019). Subsequently, in order to make contact with literature and further clarify the origin of the hardening response, we also compare in the same section the M-Voronoi with honeycomb materials. We close the experimental section with selected anisotropic M-Voronoi results. In Section 5, triangular, trapezoidal and rectangular M-Voronoi cells are seamlessly assembled to design a complex structure with variable porosity at different regions. The conclusions are drawn in Section 6.

2. Material methods

This section describes the computational morphogenesis process and its major steps to obtain the M-Voronoi porous materials. As a first attempt, we focus on voided materials that exhibit a two-dimensional random geometry. Those are then extruded in the third (out-of-plane) dimension for subsequent 3D-printing and mechanical experiments.

2.1. M-Voronoi morphogenesis method

The proposed process consists of four main steps, which are discussed in the following and are also summarized in Fig. 1.

Step 1 *: Construction of the initial porous cell.* The proposed void growth process begins with the construction of an initial porous unit-cell (Fig. 1). We note that the unit dimensions of the cell are inconsequential and are only chosen for simplicity. It is noted here that the choice of the initial void distribution and cell geometry affects, in general, the final porous geometry obtained via this process, as it will be shown below. For illustration purposes at this stage, a square unit-cell occupying the volume $\mathcal{V}_0$ in the undeformed (reference) configuration is considered. The unit-cell comprises a random distribution of voids at initial volume fraction c_0, or equivalently at initial relative density $\rho_0 \equiv 1 - c_0$ (see Appendix). The voids may be of any shape, size or orientation (e.g., ellipsoidal or even non-convex). Here, for simplicity and numerical efficiency, the RSA algorithm developed in Segurado and Llorca (2002) and Lopez-Pamies et al. (2013) is used to embed, randomly and uniformly (in the sense of Torquato (1997, 2002)), circular holes of equal size in the square domain. Nevertheless, the proposed morphogenesis approach is general and thus any initial void geometry may be used to increase the final inclusion volume fraction (e.g. one may start with spinodal geometries at small volume fraction Maskery et al., 2017; Portela et al., 2020; Zerhouni et al., 2021).

Step 2 *: Uniform displacement boundary conditions.* The unit-cell is subsequently subjected to uniform Dirichlet (affine) displacement boundary conditions over the entire cell boundary $\partial\mathcal{V}_0$ (Fig. 1). For clarity, the most important finite strain kinematics and constitutive laws used in this work are hereinafter recalled. The deformable unit-cell occupies a volume $\mathcal{V}_0$ in the undeformed (Lagrangian) configuration with boundary $\partial\mathcal{V}_0$. We use $\mathbf{X} \in \mathcal{V}_0$ to denote the reference position vector of a material point in $\mathcal{V}_0$. The deformed position vector $\mathbf{x}(\mathbf{X})$ of any material point is related to $\mathbf{X}$ via $\mathbf{x}(\mathbf{X}) = \mathbf{X} + \mathbf{u}(\mathbf{X})$, where $\mathbf{u}(\mathbf{X})$ denotes the displacement vector of any material point. The deformation gradient is defined then as $\mathbf{F} = \partial\mathbf{x}/\partial\mathbf{X} = \mathbf{I} + \mathrm{Grad}\mathbf{u}$, where Grad denotes the gradient operator with respect to $\mathbf{X}$. We then impose the Dirichlet boundary conditions

$$\mathbf{u} = (\mathbf{F}^{\mathrm{app}} - \mathbf{I})\,\mathbf{X}, \qquad \forall \mathbf{X} \in \partial\mathcal{V}_0, \tag{1}$$

where $\mathbf{F}^{\text{app}}$ is a prescribed, constant, *non-symmetric* second-order tensor with four and nine independent components in 2D and 3D, respectively. By virtue of the divergence theorem, one may easily show that $\mathbf{F}^{\text{app}}$ corresponds to the average deformation gradient in the entire cell, i.e., $\mathbf{F}^{\text{app}} = |\mathcal{V}_0|^{-1} \int_{\mathcal{V}_0} \mathbf{F}(\mathbf{X}) \mathrm{d}\mathbf{X}$ (Hill, 1963). It is further noted that the deformed volume of the unit-cell, $\mathcal{V}$, is entirely defined in terms of the average deformation gradient $\mathbf{F}^{\text{app}}$ from the purely kinematic relation $\mathcal{V} = \det \mathbf{F}^{\text{app}} \mathcal{V}_0$. Given that the initial unit-cell is porous and thus compressible, a $\det \mathbf{F}^{\text{app}} > 1$ readily leads to an increase of $\mathcal{V}$. A second condition for the growth of voids is provided next.

Step 3 *: Nonlinear elastic energy minimization.* Subsequently, we trigger the mechanical growth of the voids by solving numerically a finite-strain (Fig. 1), nonlinear elastic boundary value problem (BVP), whose geometry is defined in Step 1 and applied boundary conditions in Step 2. For this, we use the finite element (FE) method since the geometry is extremely complex and involves large deformations leading to a non-analytical BVP. In this study, the commercial FE solver ABAQUS (Dassault Systems) is used and finite strains are enabled by the option `NLGEOM`. Moreover, quadratic six-node, plane-strain (2D) hybrid elements (`CPE6H`) are used to deal with incompressibility.

Specifically, the void phase has zero energy density and thus is simply modeled as empty with traction-free boundaries and is not meshed, while the solid phase (blue in Fig. 1) is assumed to follow an incompressible, neo-Hookean law described formally by the Helmholtz free energy density

$$W(\mathbf{F}) = \frac{\mu}{2}(\mathbf{F} \cdot \mathbf{F} - d), \quad \text{such that} \quad C(\mathbf{F}) = \det \mathbf{F} - 1 = 0, \tag{2}$$

with $d = 2, 3$ depending on the dimensionality of the problem. In this last expression, μ denotes the shear modulus and its value may be set equal to unity for the purposes of this study, while the incompressibility constraint $C(\mathbf{F})$ needs to be imposed everywhere in the solid phase. Then, the solution of the BVP is formally defined in terms of the optimization problem

$$\{\mathbf{u}, p\} = \arg \left\{ \min_{\mathbf{u}^* \in \mathcal{K}(\mathbf{F}^{\text{app}})} \max_{p^*} \int_{\mathcal{V}_0} W(\mathbf{F}(\mathbf{u}^*)) \mathrm{d}\mathbf{X} \right\} \tag{3}$$

where $\mathcal{K}(\mathbf{F}^{\text{app}}) = \{\mathbf{u} : \text{regular}, \mathbf{u} = (\mathbf{F}^{\text{app}} - \mathbf{I})\mathbf{X}, \quad \forall \mathbf{X} \in \partial\mathcal{V}_0\}$ and p is a scalar pressure field (acting as a Lagrange multiplier to impose the incompressibility constraint $\det \mathbf{F} = 1$). The corresponding first Piola–Kirchhoff stress is given by

$$\mathbf{S} = \frac{\partial W}{\partial \mathbf{F}} - p \frac{\partial C}{\partial \mathbf{F}} = \mu \mathbf{F} - p \mathbf{F}^{-T}. \tag{4}$$

Even though the solid phase is incompressible, the embedded voids are fully compressible and can grow or shrink under large deformations. By prescribing $\det \mathbf{F}^{\text{app}} > 1$, the volume of the unit-cell is forced to grow, which can only occur via void growth. Specifically, using the incompressibility of the solid matrix phase, mass conservation and the applied Dirichlet boundary conditions, one may readily show that the current relative density of the deformed unit-cell ρ is simply given in terms of the overall initial relative density ρ_0 via the purely kinematic relation (see Appendix)

$$\rho = \frac{\rho_0}{\det \mathbf{F}^{\text{app}}}. \tag{5}$$

Equivalently, this last relation allows to estimate directly the $\det \mathbf{F}^{\text{app}}$ that needs to be prescribed to the unit-cell to reach the desired final relative density ρ. Note that $\det \mathbf{F}^{\text{app}}$ does not define the entire tensor $\mathbf{F}^{\text{app}}$. Thus, one has countless choices for the remaining components allowing to obtain a multitude of void-grown geometries and deformed cell shapes. As can be easily observed in the example problem in Fig. 1, the voids grow substantially exhibiting convex, polygonized but smooth shapes. Their exact growth rate and final shape are a complex outcome of interactions with neighboring voids and the boundary of the cell. The thickness of the intervoid ligaments is highly variable, while dense pockets of solid phase are observed across the cell, as shown by the blue spot regions in Step 3 of Fig. 1). It is also important to note that at such large strains the underlying mesh may be significantly distorted at various regions (see the zoom image in Step 3 of Fig. 1)). In order to avoid such problems, one may remesh the geometry (see remeshed figure) without the need to transfer the stress and displacement fields and re-start the calculation from that point on. This is obviously allowed here since we are solely interested in the geometrical features and not in the calculated stresses themselves. Such an operation will allow us to reach very low relative densities as is discussed in Section 2.3.

Step 4 *: Void geometry extraction, rescaling, remeshing and 3D-printing.* The deformed unit-cell is then *uniformly* rescaled back to any desired size (see Fig. 1). By doing so, the relative density is preserved. For this re-scaling step and for subsequent accuracy in 3D-printing, the following strategy is proposed, without that being neither unique nor optimal in the sense of speed. Specifically, the nodal coordinates of the external and internal void boundaries of the unit-cell are first extracted and then rescaled uniformly. The deformed mesh is exported using an Abaqus python script and the geometrical entities, such as void boundaries and cell boundaries, are read by a custom made code. It is also remarked at this point that one could use an intermediate deformation state as the initial geometry. In this case, every rescaled geometry resulting from Step 4 could be plugged in back to Step 2 to apply a new deformation history. The various options are countless. The rescaled unit-cell obtained in Step 4 is then remeshed and extruded in the third dimension. This step is conducted using the open-source meshing software *Gmsh*. It is further noted that during the remeshing operation, we do not transfer the computed displacement and stress fields, instead only the deformed cell and void boundaries are retained. Finally, the extruded geometry is exported in stereolithography (STL) format for 3D-printing. The experimental methods used to fabricate and test the samples are discussed in detail in Section 3.

2.2. M-Voronoi morphogenesis in convex cell domains

The discussed morphogenesis process is employed to obtain M-Voronoi geometries in rectangular, circular and triangular domains (Fig. 2). For simplicity in presentation, we specialize to diagonal deformation loads, i.e., $\mathbf{F}^{\text{app}} = \text{diag}(\lambda_1^{\text{app}}, \lambda_2^{\text{app}})$ (with $\lambda_1^{\text{app}}, \lambda_2^{\text{app}}$ denoting the applied principal stretches).

In Fig. 2a, we begin with a large number of initially circular voids ($\rho_0 = 0.9$), and subject the unit-cell to equi-biaxial tension with $\lambda_1^{\text{app}} = \lambda_2^{\text{app}} = \lambda^{\text{app}} > 1$. Three rescaled contours show the maximum local principal logarithmic strain at current relative density $\rho = 0.7, 0.5, 0.3$ (Fig. 2b–d). The circular voids gradually polygonize, albeit remaining smooth. This smoothness is a key feature of these newly obtained inclusion geometries. In particular, the complex interactions resulting from the disordered distributions of the voids and the underlying nonlinear large elastic deformations lead to convex and non-canonical Voronoi-type shapes. Most of these shapes resemble a pentagon and are of fairly similar size. By contrast, due to the random distance of the centers of the original circular voids, the deformed intervoid ligaments exhibit a rather random thickness variation. Pockets of almost *undeformed* solid regions (indicated by the blue spots in e.g., Fig. 2c) are formed. Those pockets gradually shrink with further increase of the applied strains (Fig. 2d). As a second representative example, the proposed morphogenesis process is employed to design M-Voronoi geometries with anisotropy. Specifically, as shown Fig. 2e–h, we apply a biaxial tension with $2\lambda_2^{\text{app}} = \lambda_1^{\text{app}} = \lambda^{\text{app}} > 1$. Such a load transforms the initial square to a rectangle and the initially circular voids to *elongated* Voronoi-type shapes. Similar to the previous equi-biaxial case, the intervoid ligaments are again non-uniform. The possibilities for designing such M-Voronoi obviously are limitless since any combinations of the $\mathbf{F}^{\text{app}}$ components can lead to different void formations and anisotropies. A selected set of such anisotropic M-Voronoi are discussed later in Section 4.4. This case of anisotropic M-Voronoi reveals the versatility

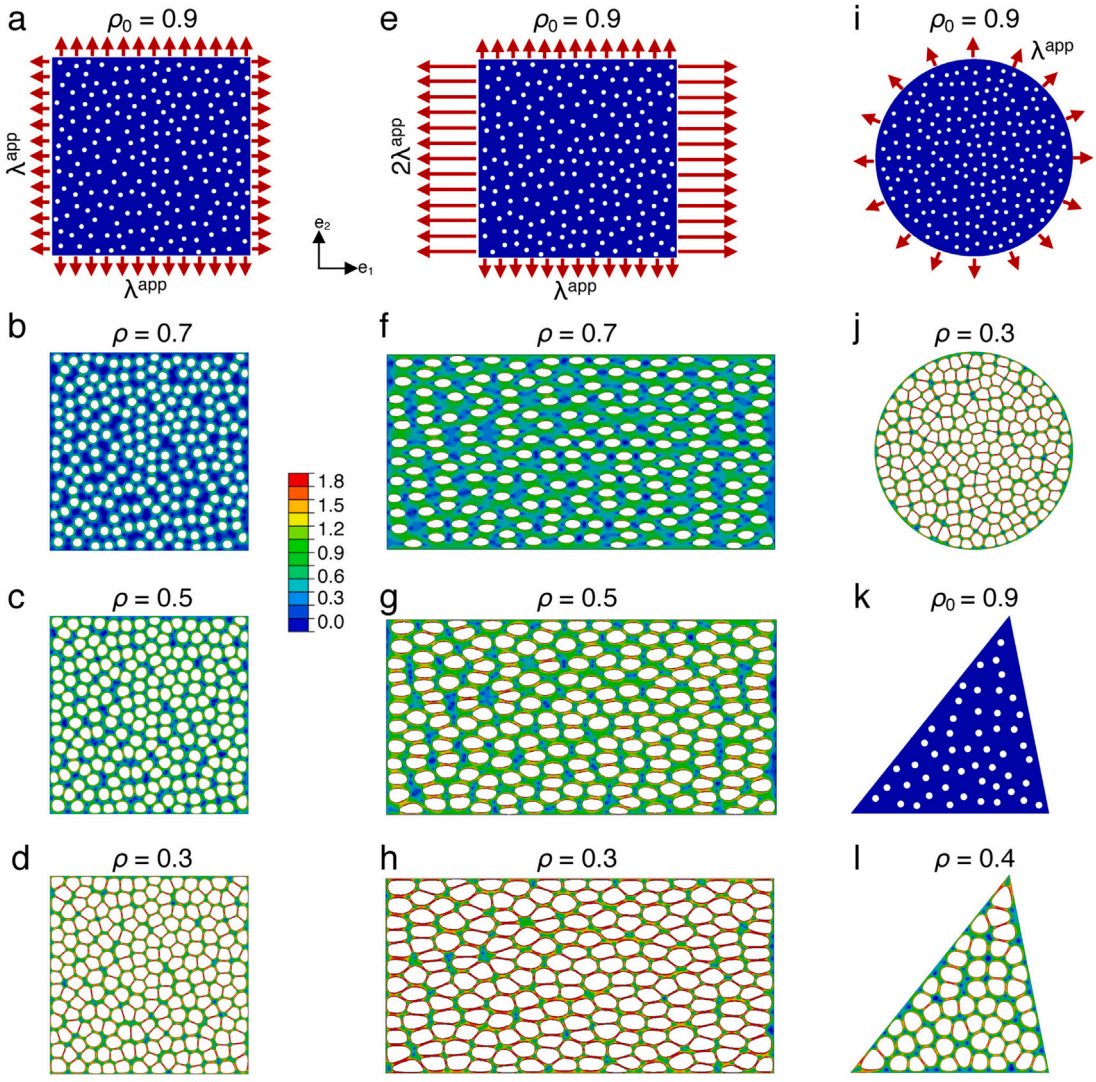

Fig. 2. Representative M-Voronoi porous geometries for porous domains with different shapes: (a-d) isotropic geometries obtained using a rectangular cell subjected to equi-biaxial tension ($\lambda_1^{app} = \lambda_2^{app} = \lambda^{app} > 1$); (e-h) anisotropic geometries obtained using a rectangular cell subjected to biaxial tension ($2\lambda_2^{app} = \lambda_1^{app} = \lambda^{app} > 1$) and isotropic geometries obtained using respectively a (i-j) circular and a (k-l) triangular cell subjected to equi-biaxial load. The initial geometries in (a), (e), (i) and (k) are obtained using the RSA algorithm and monodisperse circular voids at relative density $\rho_0 = 0.9$. All deformed cells are scaled for visualization reasons. (For interpretation of the references to color in this figure legend, the reader is referred to the web version of this article.)

of the method. This allows for a more tunable response by employing an inverse design protocol, albeit in a large nonlinear strain framework.

Finally, the simplicity of the process and the prescribed boundary conditions allows to grow M-Voronoi geometries in initially circular (Fig. 2i,j), triangular (Fig. 2k,l) or any other type of convex domain cells.[1] The applied stretches may be chosen to be equi-biaxial retaining the original shape of the domain or simply biaxial leading to anisotropic responses. Interestingly, the grown voids exhibit similar polygonal (pentagon) type features except for a few ones that lie very close to the boundaries. For instance, the voids lying near the circle periphery or the corners of the triangle take a rather triangular shape (Fig. 2l). The use of equi-biaxial loads tends to lead to a more isotropic growth even in anisotropic domains such as the triangular one. In turn, the use of non-equi-biaxial loads triggers a direction-dependent (i.e. anisotropic) void growth. In all cases, the only constraint that needs to be imposed for positive void growth is simply $\det \mathbf{F}^{app} > 1$, while the remaining components of $\mathbf{F}^{app}$ may be arbitrarily chosen. It is important to note, that the randomness of void distributions allows to "fill" efficiently and uniformly those domains with voids/inclusions, a process that would be extremely difficult to achieve with periodic geometries (such as honeycombs, periodic lattices, etc.).

2.3. E-Voronoi and RSA versus M-Voronoi

For later use, we examine now the differences between the M-Voronoi geometries proposed in the present work versus the E-Voronoi and RSA polydisperse geometries (Fig. 3). The (eroded) E-Voronoi geometries (Fig. 3a) are constructed by use of the algorithms presented in Spyrou et al. (2019) for the modeling of human muscles. In that study, a standard Voronoi tessellation is first created and subsequently the walls of each Voronoi inclusion are eroded in a uniform manner leading to constant-thickness intervoid ligaments. The amplitude of erosion defines the final relative density, while the intervoid ligaments are meshed in two-dimensions to reach arbitrary values of ρ (as opposed to earlier studies such as in Tekoglu et al. (2011) where beam elements

[1] Even though it is not shown rigorously, it is rather intuitive to see that a non-convex initial geometry of the unit-cell would lead to contact of the exterior faces of the cell and subsequent cease of the simulation under uniform affine loads. Thus a convex cell geometry, albeit of arbitrary shape is essential at the initial stage.

were used). By construction, the E-Voronoi void boundaries exhibit sharp corners, while the process may lead to locally more elongated inclusions of large aspect ratio towards an arbitrary direction. The E-Voronoi geometries can span the entire range of practical relative densities from 0 to very low (e.g., 0.01) and are isotropic as a direct consequence of the random Voronoi tessellation process (but see the recent extension to anisotropic ones by van Nuland et al. (2021)). The random adsorption algorithm (RSA) geometries (Lopez-Pamies et al., 2013) contain multiple sized (i.e. polydisperse) circular voids that are embedded randomly in the square domain (Fig. 3b). Similar to the M-Voronoi, the RSA geometries exhibit non-uniform intervoid ligament thickness, while being extensively polydisperse with decreasing relative density. The main challenge in constructing the RSA geometries lies in the fact that it becomes increasingly difficult to reach representative specimens in the nonlinear finite-strain regime with very low relative densities (less than 0.2 in 2D and less than 0.3 in 3D) that are realizable numerically (for instance, no geometry has been achieved for $\rho = 0.01$ as shown in Fig. 3b) as well as with 3D-printing technology. This is due to the extremely large difference between the largest and the smallest voids necessary to achieve such low densities. In turn, the RSA geometries may be isotropic or anisotropic depending on the void shapes (Anoukou et al., 2018) (e.g. ellipsoidal shape) and their distribution. In the present work, we focus on circular voids distributed randomly and uniformly in the square cell leading to a fairly isotropic response.

By contrast, the proposed M-Voronoi geometries are numerically and experimentally realizable at solid densities spanning the full spectrum from 1 to very low (e.g., 0.01) (Fig. 3c–e). For conciseness, we report M-Voronoi geometries obtained via an equi-biaxial loading history. We show that the initial relative density, ρ_0, affects strongly the final M-Voronoi geometry. A higher initial $\rho_0 = 0.9$ (Fig. 3c) leads to substantially more uniform and equi-sized Voronoi inclusions contrary to a lower initial $\rho_0 = 0.7, 0.5$ (Fig. 3d,e). The latter tend to create disordered clustering of smaller and larger voids randomly distributed in the cell. It is important to note at this point that in order to achieve very low relative densities such as $\rho = 0.01$ while avoiding excessive mesh distortions, it is preferable to stop the simulation at an intermediate value of ρ, e.g. $\rho = 0.1$, extract the geometrical characteristics, remesh and re-launch the simulation to reach the final relative density desired. This last process implies re-launching Steps 1-3 discussed in Fig. 1, but using an intermediate M-Voronoi geometry as an initial one. Obviously this process can be repeated whenever necessary to avoid severe mesh distortion or numerical convergence issues.

3. 3D-printing and experimental methods

3.1. 3D-printing interruption strategy

The present porous test specimens with increasing porosity are 3D-printed via a PolyJet technology, using an EDEN 260VS printer from Stratasys and a rubber-like UV-curable resin (commercial name TangoBlack FLX 930 from Stratasys). Although not required in the present work, we have performed independent uniaxial tension tests of TangoBlack specimens at very slow strain-rates ($7 \cdot 10^{-4}$ s^{-1}) leading to a neo-Hookean response up to fracture (occurring at strains less than 20%) with an initial Young's modulus of 3.92 MPa and Poisson's ratio 0.49.

Prior to the manufacturing of the porous specimens, a straightforward 3D-printing test (not shown here for brevity) using isolated and closely packed aligned circular, cylindrical voids was conducted to quantify the size of the pore features that could be manufactured with sufficient geometrical accuracy. Therein, we find that the minimum pore diameter and intervoid thickness ligament that may be 3D-printed once-off with acceptable accuracy are respectively, ~300 μm and ~600 μm. These numbers are slightly larger than those reported in a study considering RSA geometries with VeroWhite material (Tarantino et al., 2019).

For the experimental study, and in order to attain with our 3D-printer the minimum ligament thicknesses required for representativity of the results discussed in detail in Section 4.1, we consider porous test specimens with in-plane dimensions $100 \times 100\,\text{mm}^2$ and out-of-plane thickness 10 mm. In the M-Voronoi materials, we do not control entirely the thickness of the intervoid ligaments. In fact, those are highly variable at different positions. As a result, as one reaches lower relative densities, the intervoid ligament thickness may become less than the minimum that can be accurately 3D-printed (i.e., < 300 μm) resulting to a rather low quality reproduction of the numerically obtained geometrical features, especially along the out-of-plane direction, as shown Fig. 4a. In order to improve further upon this limitation directly related to the specific 3D-printing technology used, we propose here an interruption strategy. In the present case of a commercial 3D-printer, this simply consists in manually interrupting the 3D-printing process for a few minutes thus allowing the existing polymer layer to solidify partially before additional layers with additional weight are positioned atop. As clearly shown in Fig. 4b, this interruption strategy allows to improve substantially on the quality of the 3D-printed specimen, even though some imperfections are still present in these extreme relative densities. For completeness, we also include in Fig. 4c,d, corresponding E-Voronoi geometries. Even in this case of uniform intervoid ligament thickness, we observe that an once-off 3D-printing approach still leads to imperfections, albeit of smaller amplitude than those observed for the M-Voronoi geometries.

More precisely, the interruption period depends on the in-plane dimensions of the specimen and the number of specimens laid on the 3D-printer tray. The reason for this is simply related to the time that the 3D-printer heads require to return to exactly the same printing point. As a rule of thumb in our work, we use the following time steps. For one specimen of in-plane dimensions $100 \times 100\,\text{mm}^2$, we 3D-print for 10 min and interrupt for another 10 min. Given that the total estimated time for a single-step 3D-printing of the given specimen with out-of-plane thickness of 10 mm is about 1 h, the interruption delay time is taking place every about 10/6 mm intermediate layers. If additional specimens are added in the tray, the 3D-printing time before applying an interruption should be calculated accordingly. Obviously, the proposed time scales do not constitute a universal protocol expected to work for any arbitrary geometry. Nevertheless, the idea itself of interruption clearly allowed us to improve the quality of the 3D-printed specimens especially at low relative densities.

For completeness, we show in Fig. 5, 3D-printed specimens for $\rho = 0.2$ for all three geometries, i.e., (a) M-Voronoi, (b) E-Voronoi and (c) RSA. In this case, no interruption during the 3D-printing is necessary to achieve sufficient specimen quality. Even so, one may observe at the boundaries of the cell a few regions where the 3D-printing has not been entirely complete. Nevertheless, those regions are only a very minor proportion of the specimen and they do not affect the overall response, as we will show in the representativity study in Section 4.1.

3.2. Testing protocol

The 3D-printed test specimens are subjected to quasi-static uniaxial compression using a servo-hydraulic testing machine and their deformation history is tracked by means of a CCD camera. Experiments are carried out under displacement control with a constant strain rate of $0.001\,\text{s}^{-1}$. For the measurement of the force signal, two different load transducers with capacity 200 ± 0.002 N and 10 ± 0.001 N are employed depending on the relative density of the test specimen. Specifically, the 200 N transducer was mounted onto the fixed platen of the testing machine, whereas the 10 N transducer (mounted onto the movable platen of the crosshead) is designed to double as a piston. To this end, a dedicated testing set-up proposed in Tarantino and Danas (2019) is re-adapted and used. Finally, during experiments all specimens are

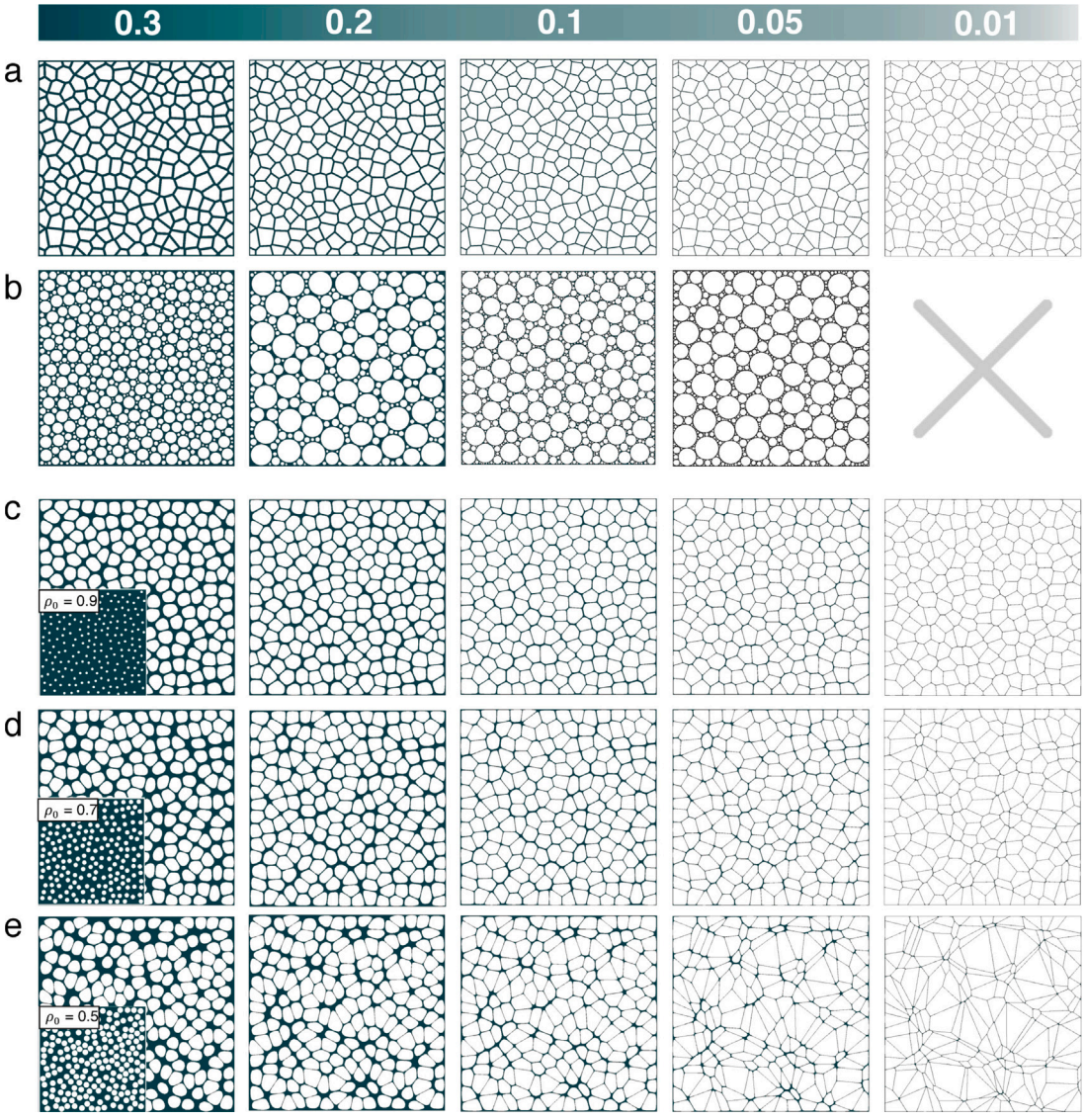

Fig. 3. (a) E-Voronoi. (b) RSA polydisperse circles. (c-e) M-Voronoi obtained by using a RSA geometry with initial relative density (c) $\rho_0 = 0.9$, (d) $\rho_0 = 0.7$ and (e) $\rho_0 = 0.5$ as shown in the insets of the first row. The $\rho = 0.01$ geometries in (c-e), are obtained by using the corresponding $\rho = 0.1$ as an initial geometry after remeshing it. The top color bar indicates the final relative density ρ. (For interpretation of the references to color in this figure legend, the reader is referred to the web version of this article.)

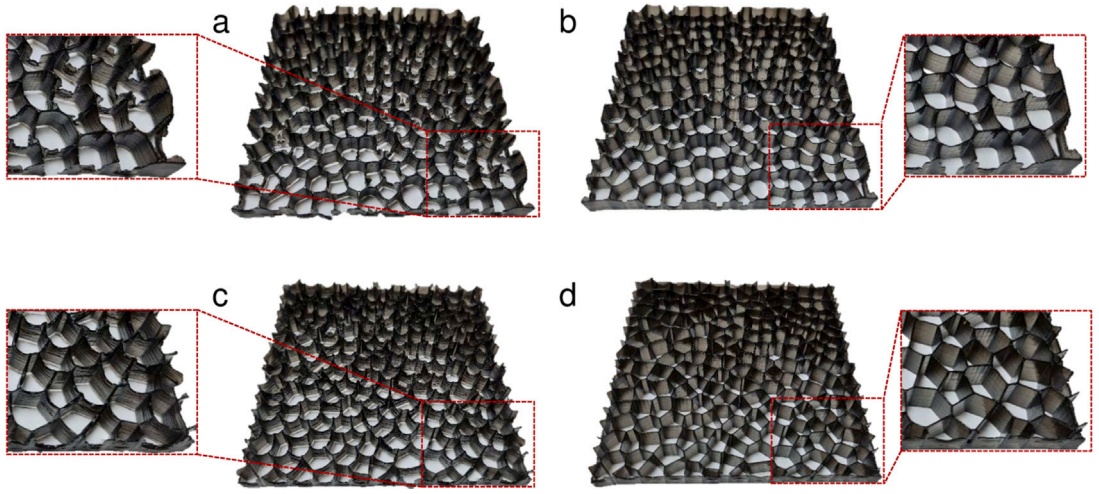

Fig. 4. (a,b) M-Voronoi and (c,d) E-Voronoi 3D-printed specimens with relative density $\rho = 0.1$. The specimens are obtained in (a,c) without and (b,d) with the interruption strategy.

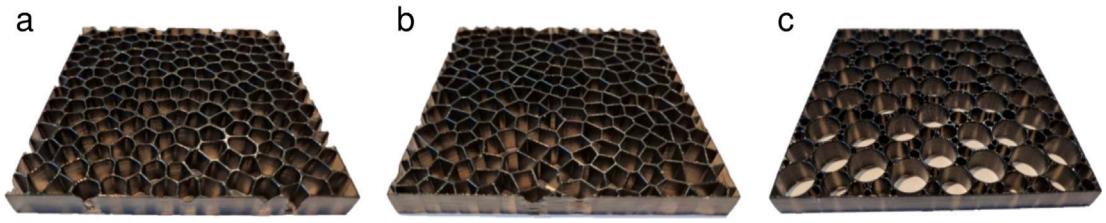

Fig. 5. (a) M-Voronoi, (b) E-Voronoi and (c) RSA 3D-printed specimens with no interruption strategy and $\rho = 0.2$.

enclosed between two transparent PMMA plates of 10 mm thickness in order to avoid out-of-plane-buckling of the test specimens. The two plates are lubricated with teflon at the inner side to reduce contact friction with the test specimen.

4. Experimental results and discussion

In this section, we quantify experimentally the response of the M-Voronoi, E-Voronoi and RSA geometries when subjected to uniaxial compression loads. First, we study the representativity and isotropy of response of the M-Voronoi (the E-Voronoi have a similar response to the M-Voronoi in terms of representativity) and RSA specimens in terms of number of voids as well as direction of loading (in order to probe isotropy even partially). Subsequently, we carry out a comparison analysis between the M-Voronoi, E-Voronoi and RSA geometries for isotropic and anisotropic geometries.

4.1. Representativity and isotropy of M-Voronoi

Considering the previously-mentioned fabrication constraints, we choose the overall size to be $100 \times 100 \times 10\,\text{mm}^3$ for all 3D-printed specimens. These dimensions allow to reach a large enough number of voids (~250) leading to a sufficiently representative response (i.e., scattering of the response as a function of realization and number of voids) and low relative density realizability.[2] By considering 200 voids (or ~14 per each direction) in the M-Voronoi, we obtain a minimum void diameter size of ~5 mm. Note that since the void distribution and size are random, these numbers should only be considered in an average sense. Decreasing the number of voids leads gradually to a more "structural" (i.e. with larger scatter) response that is strongly dependent on realization. In order to assess the effect of the number of voids in the cell (or equivalently void size) effect on the representativity of the response, we carry out experiments for six different numbers of voids, $N_p = 30, 50, 100, 150, 200, 250$ with $\rho = 0.3$ in M-Voronoi specimens, as shown Fig. 6.

Specifically, Fig. 6a shows the overall "engineering" stress–strain response of the relevant M-Voronoi geometries. At this stage, only one realization is considered. As easily observed in Fig. 6a, convergence of the stress–strain response is achieved as we increase $N_p \geq 200$ voids.[3] The cross-plot in Fig. 6b shows the engineering stress as a function of N_p at different levels of the strain. We conclude that beyond $N_p \geq 200$ a sufficiently converged response is obtained, as this is revealed by the saturation of the stress measures with increasing N_p. This average number of voids is used in the next sections to compare the various geometries. It is further pointed out that even in fully periodic systems such an analysis is necessary to assess the representativity of the results as a function of the specimen size. Such an analysis is even more critical at large strains where nonlinear phenomena such as buckling or fracture are involved (Michel et al., 2007).

[2] It is noted here that experimental realizability of the geometries is directly tight to the accuracy of the 3D-printer. The resulting representative geometries are, in turn, scalable and independent of the size of the specimen itself.

[3] Convergence should be thought in a less strict manner here given that in experiments scatter is also due to small fabrication variations as discussed already in Section 3.1 as well as small testing uncertainties ranging from one experiment to the other.

Table 1
Average and scatter values of the Young's modulus.

N_p	E_{ave} (kPa)	Scatter (%)
30	206	11.2
200	267	5

In order to complete the study of representativity as well as obtain a *rough* measure of the isotropy of the M-Voronoi geometries, we analyze in Fig. 7 the scatter in the stress–strain response due to different realizations but for a fixed number of voids. Figs. 7a,b correspond to $N_p = 30$ and 200 with $\rho = 0.3$. For each N_p, we consider two different realizations subjected to two different loading directions thus effectively studying four realizations, shown in Figs. 7c,d. One readily observes that increasing the number of N_p leads to a decrease of the apparent scatter. The rough convergence of the results for $N_p \geq 200$ indicates that the M-Voronoi geometries behave similarly in the two main directions of the square cell. This invariance to directionality is a strong evidence of isotropy at large strains, albeit not entirely complete. Nevertheless, a more complete isotropy analysis is not possible with our current experimental setup. Yet, considering the randomness of the geometry and the different realizations, the present results imply a sufficient isotropic response even at *large strains*, a feature usually ignored in many recent studies of plates, trusses and more generally periodic cellular materials. We recall here that isotropy in linear elasticity and small strains does not imply[4] isotropy at large strains as we show clearly in Section 4.3. It is also noted that additional geometries (not shown here for brevity) and tests were performed with open voids reaching the lateral boundaries. The latter did not change the converged response observed in Fig. 7b.

By contrast, for $N_p = 30$, while at small strains all four realizations exhibit very similar response (up to an acceptable scatter discussed in the following), their scatter increases substantially leading to a different initial buckling as well as post-bifurcated response. This observation reveals the extremely complex local mechanisms that enter in the response of the post-bifurcation regime, as well as the fact that representativity of response is strongly dependent on realization, void sizes as well as the consideration or not of large strains.

Next, we analyze the scatter induced by the different realizations discussed previously. The scatter of a quantity A is defined as

$$\text{Realization scatter } \% = \frac{A_{max} - A_{min}}{A_{ave}} \times 100. \tag{6}$$

where A_{max}, A_{min} and A_{ave} correspond to the maximum, minimum and average value of the quantity among different realizations.

In Table 1, we show the average and scatter values for the apparent Young's modulus obtained at very small strains (0–0.2%). We observe that increase of N_p leads effectively to a stiffer and less scattered response as expected.

[4] Perhaps the most straightforward example is that of two-dimensional hexagonal trusses which are studied further below. At small strains, they are exactly isotropic (Francfort and Murat, 1986), but become highly anisotropic in the post-buckling regime and finite strains (Spyrou et al., 2019).

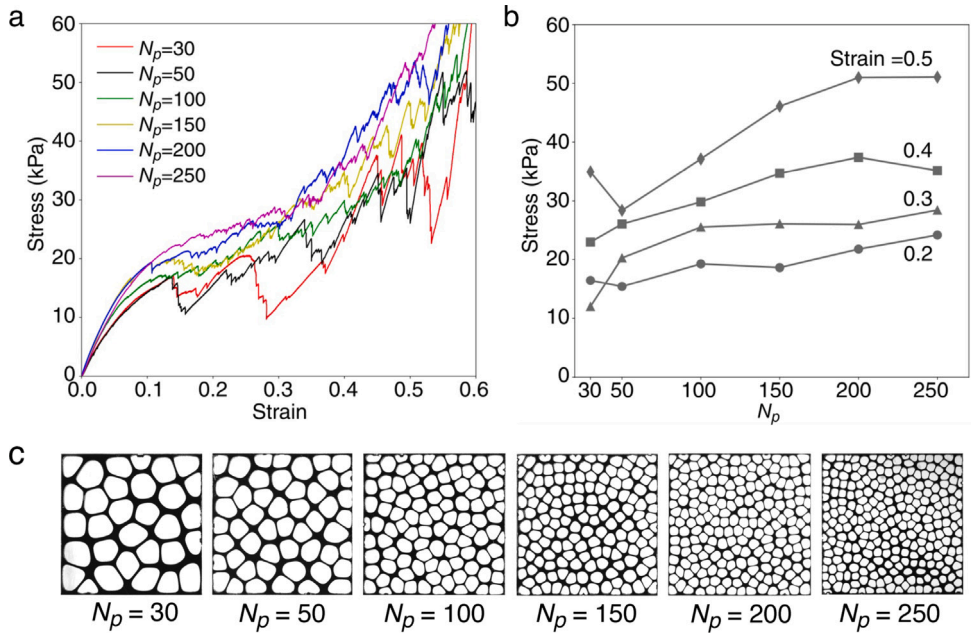

Fig. 6. Experimental representativity study for M-Voronoi with $\rho = 0.3$ in terms of number of voids N_p. (a) Stress–strain response of the M-Voronoi with different number of voids and (b) engineering stress as a function of N_p for different levels of the overall strain. (c) Optical images of the corresponding realizations for different N_p.

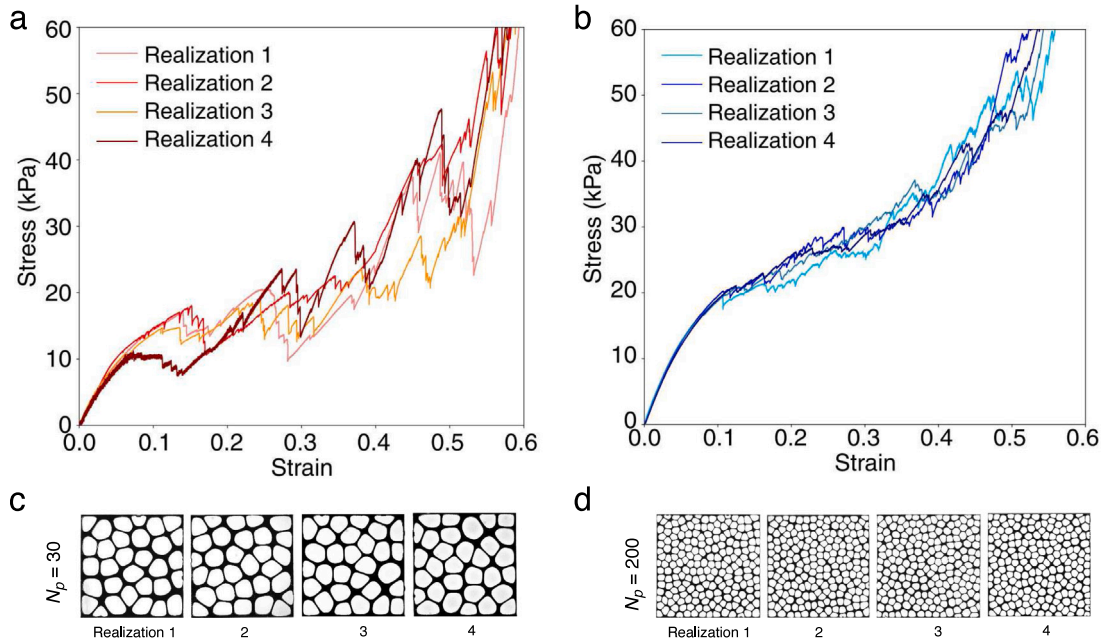

Fig. 7. Experimental representativity study for M-Voronoi with $\rho = 0.3$ in terms of number of realizations and number of voids. Stress–strain response for four different realizations for (a) $N_p = 30$ and (b) $N_p = 200$. Corresponding optical images of the realizations for (c) $N_p = 30$ and (d) $N_p = 200$.

In turn, in Fig. 8, we show the scatter of the stress values in the strain range $0.05 - 0.6$. Therein, the M-Voronoi with $N_p = 30$ are found to be highly dependent upon realization exhibiting a large scatter in the order of 40% (reaching a maximum of 90% and a minimum of 10%) while the ones for $N_p = 200$ are substantially more representative showing an average scatter in the order of 10% (reaching a maximum of 20% and a minimum of 1%) throughout the entire strain history. We should mention here that fabrication imperfections (see Section 3.1) as well as uncontrollable experimental uncertainties always lead to a certain level of scatter from sample to sample. It is clear, however, that the scatter substantially decreases with increasing number of N_p.

We close this section by noting that the RSA and E-Voronoi geometries exhibit similar behavior in terms of representativity with the M-Voronoi ones at relative densities $\rho = 0.3, 0.4$. Nevertheless, it is substantially more difficult to reach low relative densities ($\rho \leq 0.2$) and simultaneously representative responses at large strains with the RSA approach. This is a direct consequence of the necessity for a very large polydispersity ratio (i.e. difference between the largest and smallest void added in the cell) to reach low densities below $\rho = 0.2$. The difficulty is mainly linked to the limitations of our 3D-printer (e.g. the minimum ligament size that can be printed) and less of the numerical scheme itself.

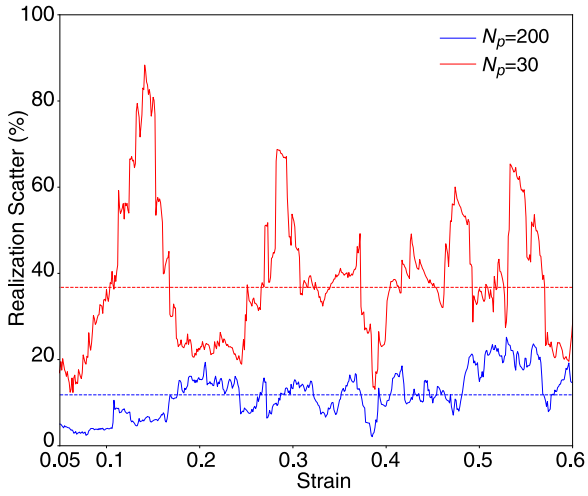

Fig. 8. The scatter in the stress–strain response induced by four different realizations of M-Voronoi geometries with $\rho = 0.3$ and number of voids $Np = 30{,}200$. The straight dotted lines indicate the average value over the strain range considered in the figure.

In order to show this clearly, Fig. 9a,b shows compression tests for RSA geometries with $\rho = 0.1$ using two different realizations subjected to two different loading directions (see Fig. 9c). Given the 3D-printing and realization constraints discussed in the previous section, we can only reach low relative densities by considering 3–4 "large" voids per-direction (with approximate size ∼15–20 mm) and many smaller ones with a polydispersity ratio in the order of ∼50/1 (Tarantino et al., 2019). Fig. 9a represents the engineering stress–strain response, while the corresponding realization scatter is shown in Fig. 9b. In agreement with earlier studies by Zerhouni et al. (2018, 2019) and Tarantino et al. (2019), at small strains, the response is rather converged and representative. Nonetheless, the initial buckling and post-buckling response becomes highly scattered at large strains. It can be observed in Fig. 9b that the amplitude of this scatter reaches very large values (∼100% at maximum). Similar representativity limitations are in general true for $\rho \leq 0.2$, and therefore their use in the next section is only done for completeness purposes.

4.2. Comparisons among the three geometries

In order to compare the three geometries considered in this study, we show in Figs. 10 and 11 quasi-static, uniaxial compression experiments for relative densities $\rho = 0.4, 0.3, 0.2, 0.1$. The representativity analysis carried out in the previous section allows to consider only one realization for the M-Voronoi geometries. In order for the comparison to be meaningful, the corresponding E-Voronoi geometries also contain a similar number of voids with the corresponding M-Voronoi ones. For a better understanding, we also include optical images of the three geometries selected at three intermediate strains levels, denoted with (1), (2) and (3).

In Fig. 10 corresponding to relative densities $\rho = 0.3, 0.4$, the initial response for all tested geometries has a net linear behavior. The range of the initial linearity decreases with decreasing relative density, as shown in Fig. 11 corresponding to $\rho = 0.1, 0.2$. In all cases however, this initial linear response remains free of oscillations. After this initial smooth behavior, initial buckling, deformation localization and fracture occur at different regions in the specimen (see green lines on the optical images). Since the tested samples are random, ligaments bend, buckle and rupture at different positions inducing an oscillatory overall response. Rather remarkably, the M-Voronoi exhibit the strongest hardening response with no apparent *major peak-stress* up to complete densification and for all relative densities considered here. This leads to overall the stiffest response at large strains, even if initially the M-Voronoi may exhibit a lower modulus than the corresponding RSA geometries in some cases (e.g., $\rho = 0.3$). In particular, for $\rho = 0.3$, the RSA geometries show an initially stiffer response than the M-Voronoi which however becomes softer at larger strains leading to a lower hardening modulus than that of the M-Voronoi at moderate and large strains. Note that in general, the RSA geometries exhibit similar trends with the M-Voronoi ones, except at lower $\rho = 0.1, 0.2$ (Fig. 11), where the response becomes non-representative for the reasons discussed in Section 4.1. As consequence, at low densities $\rho = 0.1, 0.2$, the RSA depict a more flat, plateau-type, response beyond the occurrence of the first peak-stress. Such plateau type responses are very usual in lattice, truss and plate-type models (Symons and Fleck, 2008) as well as in stochastic porous composites (Jang et al., 2008; Gong and Kyriakides, 2005). A few exceptions have been reported for random foams produced by replication processing (San Marchi and Mortensen, 2001) though.

By contrast, the E-Voronoi, even though they exhibit no major peak-stress, their stress–strain response and overall hardening rate lies always lower than that of the M-Voronoi for all relative densities considered here. To explain this further, we focus on the corresponding optical images. It is clear that the non-uniform intervoid ligament thickness of the M-Voronoi geometry leads to a diffuse distribution of buckled, bended and fractured unconnected zones throughout the entire specimen (see for instance the corresponding image in Fig. 10b for the M-Voronoi). The RSA exhibit a similar distribution of disordered and disconnected pockets of localized deformation. By contrast, the E-Voronoi cells, despite being random too, very early form a localization/fracture band that spans the entire specimen for all relative densities considered here. This is a direct consequence of the *uniform* intervoid ligament thickness. Again, such responses are also representative in periodic geometries including trusses, lattices and plate-based architected materials (Symons and Fleck, 2008). Interestingly, the E-Voronoi response approaches the M-Voronoi one at lower relative density $\rho = 0.1$. This is somehow expected since at such low relative densities the M-Voronoi samples exhibit a gradually more uniform intervoid ligament thickness, but somehow the M-Voronoi still remains superior, especially at larger strains. Note however, that at such low densities, the differences are in the order of the realization scatter. We note further that as ρ decreases, fracture becomes less dominant and the thin ligaments mainly deform by bending and stretching and less by shearing. Even so, the long-wavelength localization bands in E-Voronoi persist for all ρ considered here, while the M-Voronoi continue to exhibit more disconnected and diffuse deformation modes. Finally, it is important to note that overall the higher hardening modulus of the M-Voronoi leads to a lower densification strain than the corresponding E-Voronoi one.

4.3. Comparisons with honeycomb geometries

In this section, we compare the M-Voronoi geometries with the widely used honeycomb or hexagonal void geometries. While honeycombs are *exactly* isotropic in the linear elastic regime, they become highly anisotropic beyond buckling exhibiting a peak-stress, a pronounced plateau and subsequent densification. For this reason, the honeycombs constitute a perfect case study in the present work allowing to clarify whether the corresponding M-Voronoi hardening response at large strains is due to geometry or is strongly affected by the constitutive response of the 3D-printed polymer itself.

In Fig. 12a, corresponding to relative density $\rho = 0.4$, we observe that both the longitudinal and transverse response of the hexagonal geometries is initially linear. This linearity changes abruptly at strains of about 0.15 where the longitudinal geometry exhibits a clear peak-stress and subsequent softening due to the appearance of a localization band spanning the entire specimen (see the corresponding optical image). Beyond that peak-stress the response is oscillatory due to fracturing and the occurrence of additional localization bands. As a

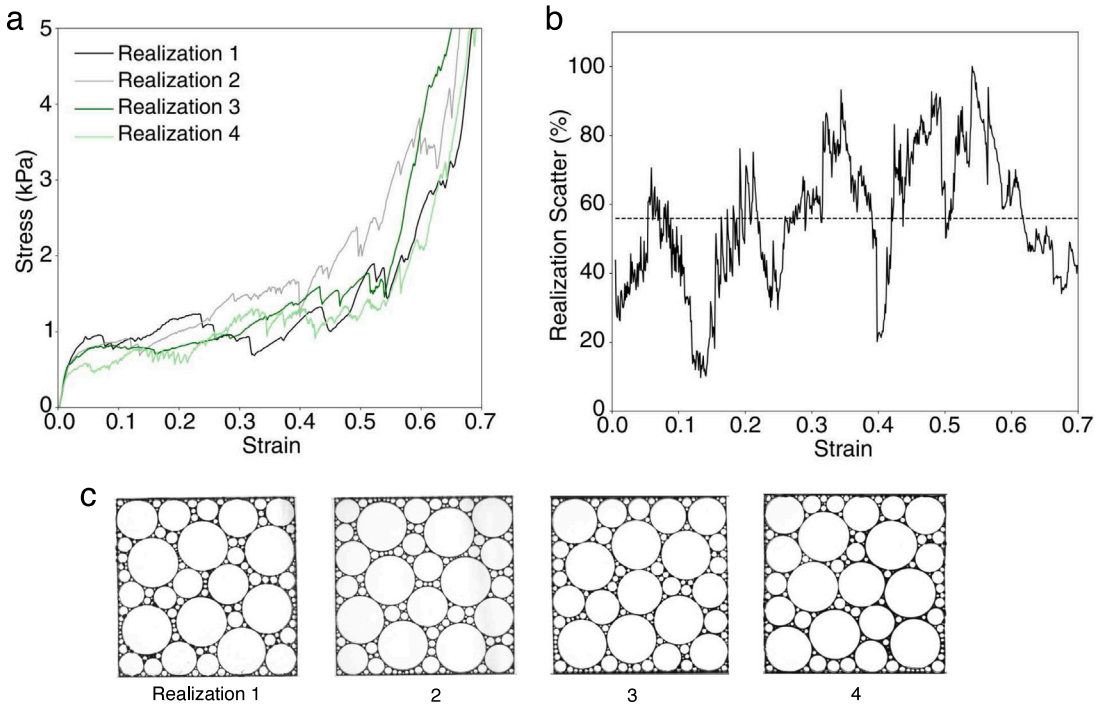

Fig. 9. Experimental representativity study for RSA with $\rho = 0.1$ in terms of number of realizations. (a) Stress–strain response for four different realizations. (b) Stress–strain realization scatter. The straight dotted line indicates the average value over the strain range considered in the figure. (c) Corresponding optical images of the realizations considered.

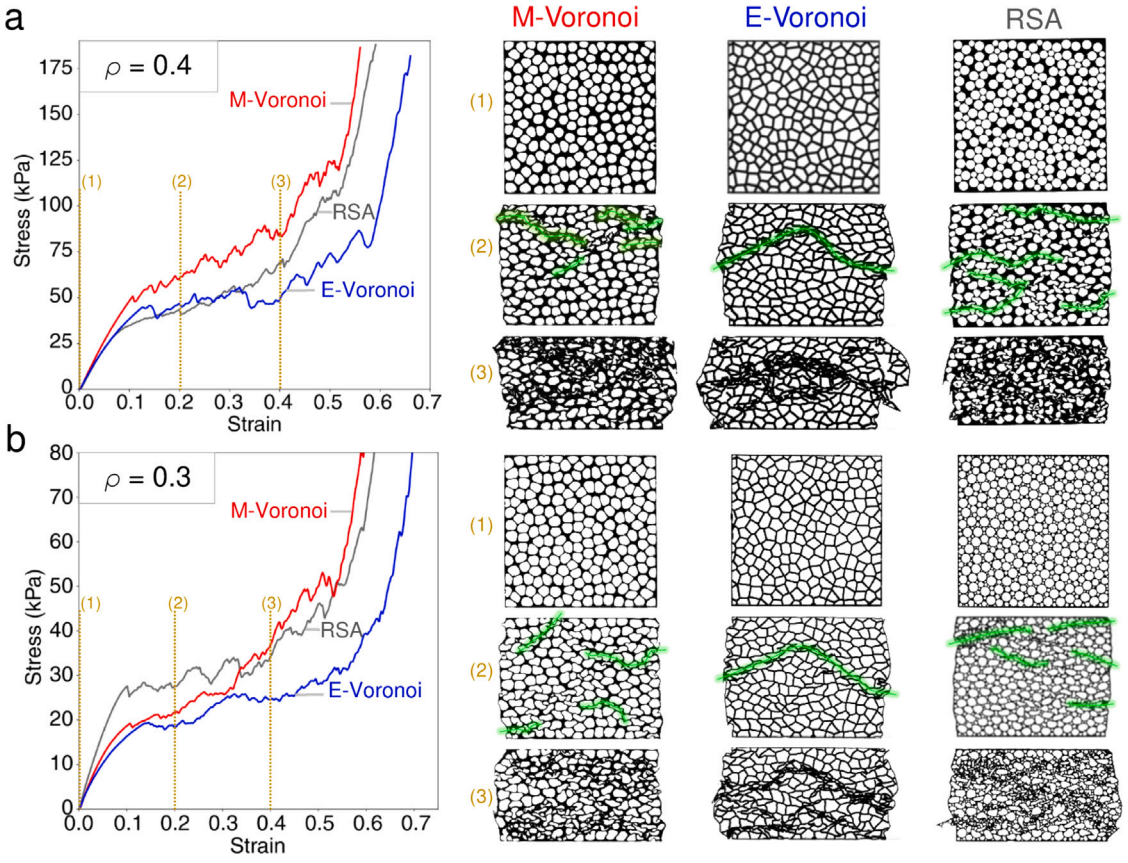

Fig. 10. Compression experiments and corresponding optical images for the M-Voronoi, E-Voronoi and RSA geometries for relative densities (a) $\rho = 0.4$ and (b) $\rho = 0.3$. For all cases, snapshots are shown of the three geometries selected at three intermediate strains levels, denoted with (1), (2) and (3). The green lines indicate zones of strong localization and fracturing of the intervoid ligaments. The in-plane dimensions of the undeformed specimens are $100 \times 100\,\mathrm{mm}^2$. (For interpretation of the references to color in this figure legend, the reader is referred to the web version of this article.)

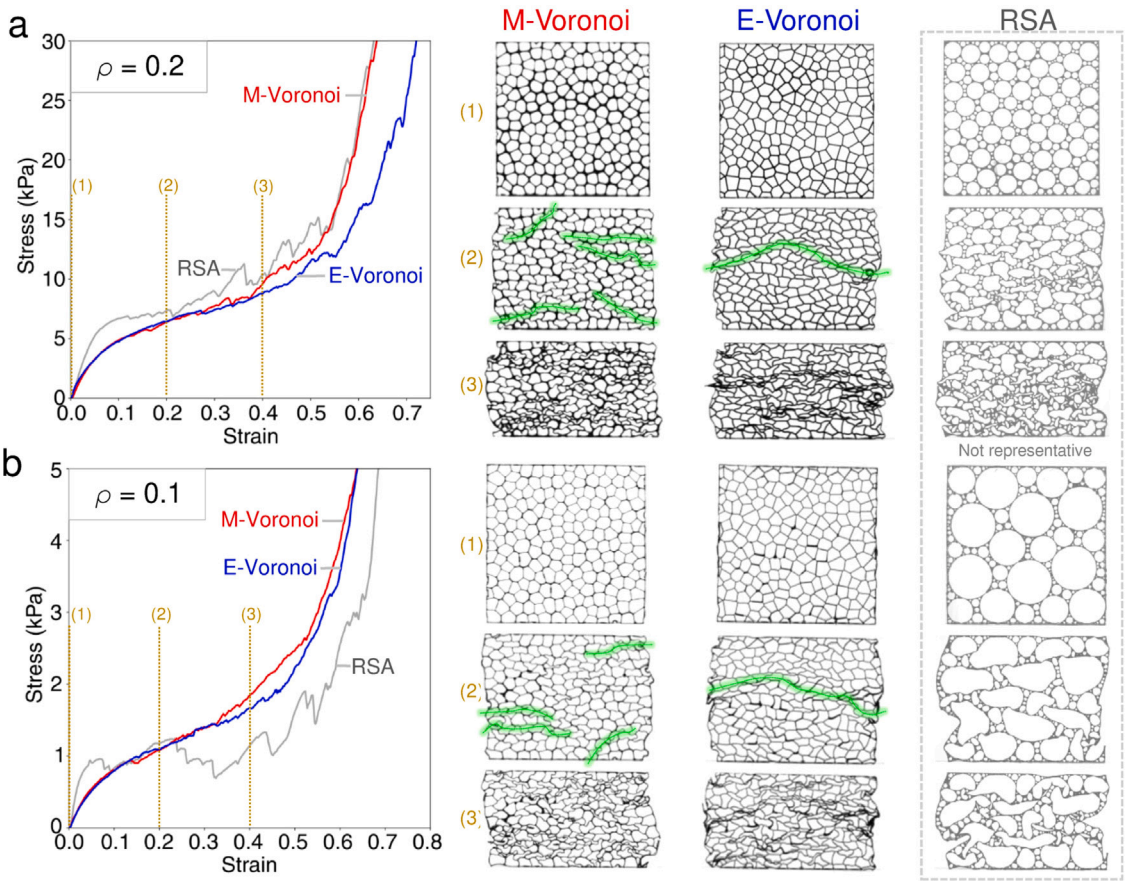

Fig. 11. Compression experiments and corresponding optical images for the M-Voronoi, E-Voronoi and RSA geometries for different relative densities (a) $\rho = 0.2$ and (b) $\rho = 0.1$. For all cases, snapshots are shown of the three geometries selected at three intermediate strains levels, denoted with (1), (2) and (3). The green lines indicate zones of strong localization and fracturing of the intervoid ligaments. The RSA for $\rho = 0.2, 0.1$ are non-representative due to fabrication limitations. The in-plane dimensions of the undeformed specimens are $100 \times 100\,\text{mm}^2$. (For interpretation of the references to color in this figure legend, the reader is referred to the web version of this article.)

result, the longitudinal honeycomb response exhibits no apparent hardening, except much later near the densification regime. By contrast, the response of the transverse honeycomb sample does not exhibit a clear peak-stress but still shows a much lower apparent hardening than the corresponding M-Voronoi geometry. Interestingly, the transverse hexagon geometry shows localization at larger strains and overall exhibits a stiffer response and hence better absorption properties than the longitudinal geometry since they both exhibit very similar densification strains. The results are qualitatively similar for $\rho = 0.3$, not shown here for brevity. Therefore, one may conclude, that for moderate relative densities $\rho \geq 0.3$, the hardening exhibited by the M-Voronoi is mainly due to its geometrical characteristics–i.e., randomness in both void and ligament size as well as the rounding of the void surfaces–and not a result of the base material hardening.

In Fig. 12b, we compare M-Voronoi with honeycombs for a lower relative density $\rho = 0.1$. The main observations made for $\rho = 0.4$ remain valid here too except for the fact that all geometries now exhibit a clear hardening less or more pronounced depending on the loading direction. A main difference between $\rho = 0.1$ and 0.4 is that at low relative densities the intervoid ligaments mainly buckle or bend but very little fracture is observed in all geometries considered here. This change of deformation mode (i.e. from shear fracturing to bending) leads to a much smoother response throughout the entire process for both the M-Voronoi and the hexagons. Rather interestingly, the longitudinal hexagonal geometry exhibits a remarkably uniform local bifurcated pattern up to very large strains showing no apparent localization band (see also Ohno et al. (2002) for corresponding theoretical results). Obviously this response is strongly related to the use of a base polymer material instead of a metallic one. In the latter case, the longitudinal hexagon geometry only shows such local bifurcated patterns in a fairly short region of straining before plastification beyond which localization bands and crushing appears (Papka and Kyriakides, 1994; Ashby and Gibson, 1997; Papka and Kyriakides, 1998). In turn, the transverse hexagon geometry exhibits localization bands originating from the boundaries in the present case.

In closing, we observe that the M-Voronoi geometry, although softer initially, overcomes both the longitudinal and transverse honeycomb curves as a result of its strong hardening. In this lower density case, as expected from the early studies of Ashby and Gibson (1997), the hardening of the polymer material leads to a slight hardening of the hexagonal geometries (see Fig. 4.2 in that reference). Yet, that mild hardening, which is a direct result of the stable post-buckling response of the honeycombs, remains substantially lower than that exhibited by the M-Voronoi. At this point, one may also comment on the possible imperfection sensitivity of the random *versus* periodic geometries. The M-Voronoi, RSA and E-Voronoi geometries are expected to be relatively insensitive to small imperfections owing to their intrinsic randomness, while it is intuitively straightforward to assume that the very uniform deformation process of the longitudinal hexagonal material in Fig. 12b may be lost under the presence of fabrication imperfections (such as missing or of varying thickness ligaments) or leading to an even less pronounced hardening response. Nonetheless, such claims need to be further confirmed by experiments along such directions. Such an analysis is beyond the scope of the present study.

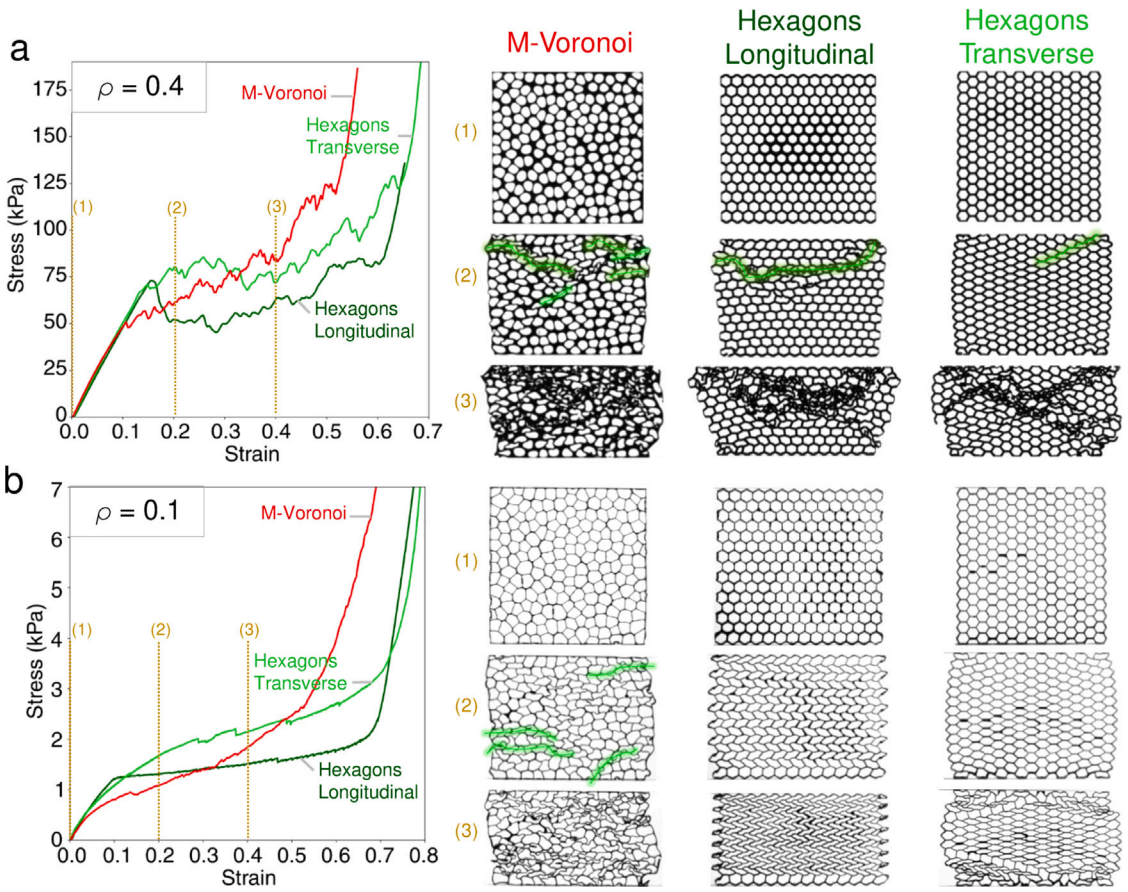

Fig. 12. Compression experiments and corresponding optical images for the M-Voronoi, Honeycombs along the longitudinal and transverse direction for two relative densities (a) $\rho = 0.4$ and (b) $\rho = 0.1$. For all cases, snapshots are shown of the three relevant geometries selected at three intermediate strains levels, denoted with (1), (2) and (3). The green lines indicate zones of strong localization and fracturing of the intervoid ligaments. The in-plane dimensions of the undeformed specimens are $100 \times 100\,\text{mm}^2$. (For interpretation of the references to color in this figure legend, the reader is referred to the web version of this article.)

4.4. Anisotropic M-Voronoi

The morphogenesis process for designing M-Voronoi geometries leads to macroscopic isotropy or anisotropy depending on the prescribed boundary conditions. As already shown in Fig. 2e-h, anisotropic M-Voronoi geometries can be obtained using a rectangular cell subjected to biaxial deformation where principal stretches are not equal $\lambda_1^{\text{app}} \neq \lambda_2^{\text{app}}$ and maintaining positive void growth via $\det \mathbf{F}^{\text{app}} > 1$.

One, however, may readily employ an inverse design protocol to achieve a final square M-Voronoi cell with final dimensions $l_1 = l_2$ through a biaxial loading applied on an initially rectangular cell with dimensions $L_1 \neq L_2$. The latter imposes a geometrical constraint on the applied deformation to obtain the target porosity. The mechanical response of the final M-Voronoi with a specific porosity is tunable and depends on the applied deformation ratio $\eta = \lambda_1^{\text{app}}/\lambda_2^{\text{app}}$. By taking into account the geometrical constraint $l_1 = l_2$, one can readily show that the deformation ratio determines entirely the aspect ratio of the initial cell via the following relation

$$\eta = \frac{\lambda_1^{\text{app}}}{\lambda_2^{\text{app}}} = \frac{L_2}{L_1}. \tag{7}$$

Here, η is an anisotropy parameter that leads to isotropic responses for $\eta = 1$ or anisotropic otherwise.

Using the last definitions together with (5), we readily obtain the following relations for the applied deformation

$$\lambda_2^{\text{app}} = \sqrt{\frac{\rho_0}{\eta\,\rho}}, \quad \lambda_1^{\text{app}} = \eta\,\lambda_2^{\text{app}}, \tag{8}$$

with ρ_0 and ρ denoting the initial and final relative density. It is important to note that void growth is achieved when $\det \mathbf{F}^{\text{app}} > 1$, which imposes the constraint $(\lambda_1^{\text{app}})^2 > \eta$, (or equivalently $(\lambda_2^{\text{app}})^2 > \eta^{-1}$).

We assess the effect of anisotropy by designing two anisotropic M-Voronoi with $\eta = 2,4$ and $\rho = 0.3$. In Fig. 13, we observe that the initial linear response of the anisotropic M-Voronoi geometries in the longitudinal direction becomes stiffer with increasing η as compared to the corresponding transverse direction as well as the isotropic one (shown again here for completeness). Subsequently, the anisotropic M-Voronoi exhibit buckling at lower stresses with increasing η in both directions but maintain a hardening response at large strains, even though the hardening slope tends to decrease with increasing η. Interestingly, one can observe that significant fracturing occurs in the longitudinal direction but substantially less in the transverse direction which is rather soft. We conclude this discussion by the most important observation in the context of this figure which is that the isotropic response, although slightly more compliant in the initial linear regime, leads to the larger buckling stress loads as well as overall the stiffest and with largest hardening rate response throughout the deformation process.

5. Application

In this section, we take advantage of the M-Voronoi growth process over a variety of domains (Fig. 2) to propose a novel modular assembly of the porous cells into macroscopic structures of arbitrary shape (Fig. 14). As an example, we consider the logo of Ecole Polytechnique, which involves an X-shape with triangular curved ends (Fig. 14a). The latter may be *discretized* in arbitrary finite volume elements (FVE)

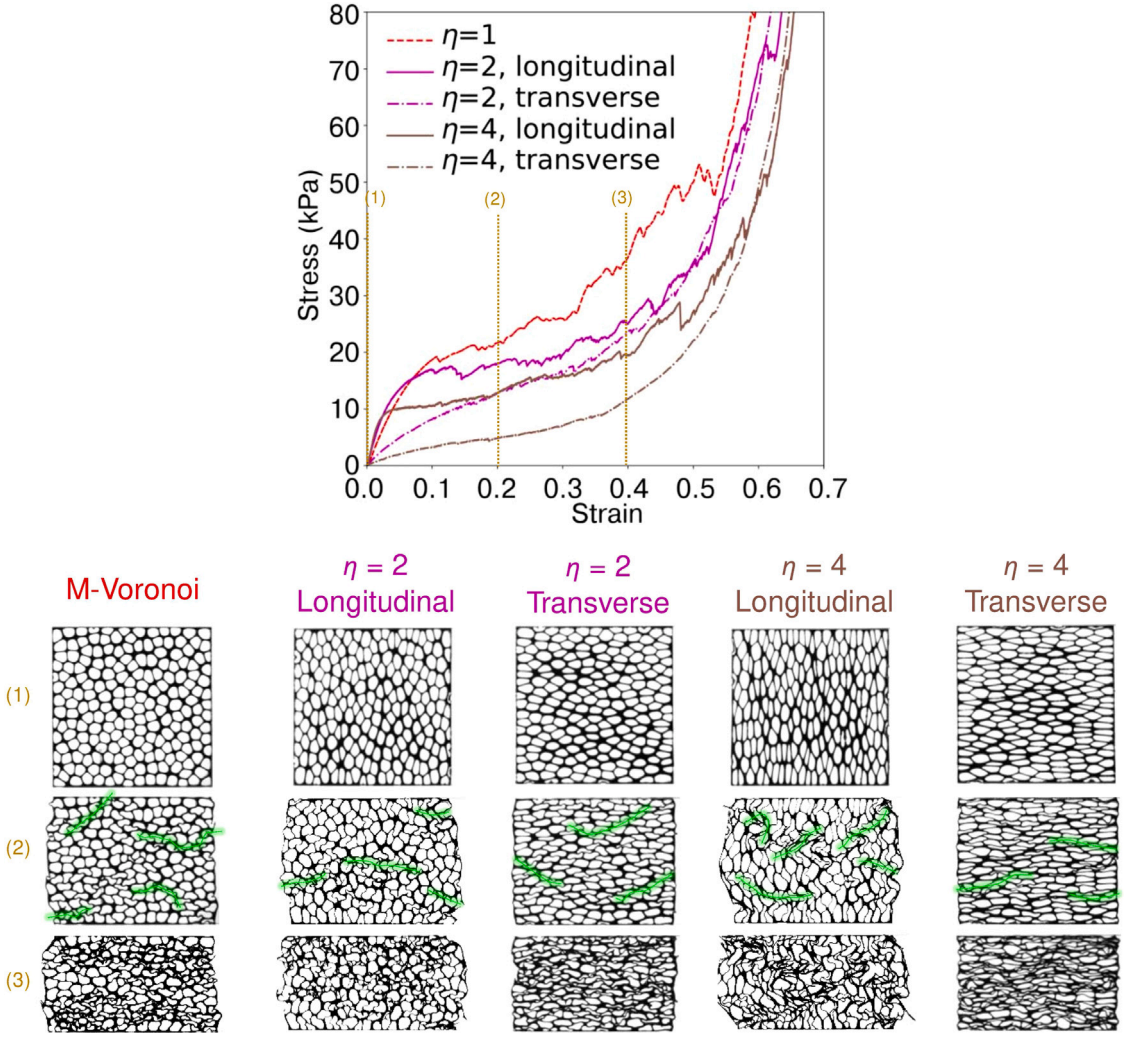

Fig. 13. Compression experiments and corresponding optical images for the isotropic and anisotropic M-Voronoi along the longitudinal and transverse direction for $\rho = 0.3$. For all cases, snapshots are shown of the three relevant geometries selected at three intermediate strains levels, denoted with (1), (2) and (3). The green lines indicate zones of strong localization and fracturing of the intervoid ligaments. The in-plane dimensions of the undeformed specimens are $100 \times 100\,\mathrm{mm}^2$. (For interpretation of the references to color in this figure legend, the reader is referred to the web version of this article.)

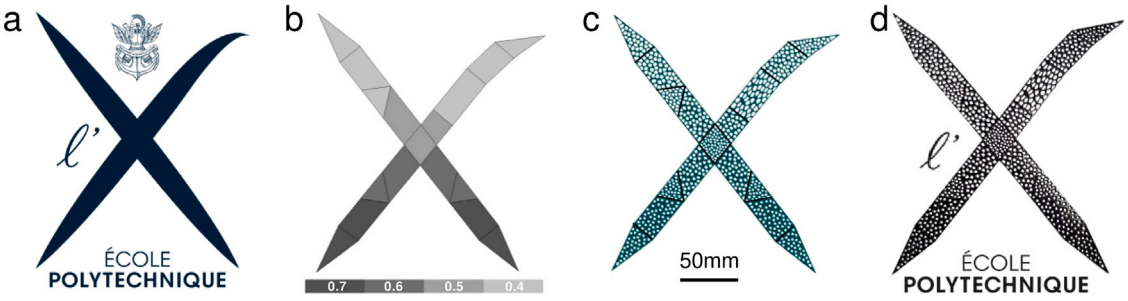

Fig. 14. Assembly of individual M-Voronoi cells into a macroscopic geometry. (a) Ecole Polytechnique Logo. (b) Finite Volume Element (FVE) discretization with arbitrary porosity and anisotropy. (c) Numerical creation and assembly of the individual porous cells. (d) 3D-printed specimen.

(similar to the finite elements in numerical methods) of triangular, trapezoidal and rectangular shape (Fig. 14b). In addition, each FVE may be attributed a different relative density and be generated by applying a different deformation history (e.g., equi-biaxial, anisotropic biaxial, or shear plus biaxial, etc.). Once created, each FVE is assembled numerically to reconstruct the original macroscopic X-shape geometry (Fig. 14c). We recall that each FVE can be uniformly rescaled at will. The final X-shape is then transformed to STL format and 3D-printed (Fig. 14d). We note that this modular assembly process is easily employed using the M-Voronoi geometries and at any relative density desired spatially. The advantage of such an assembly is that the FVEs have a versatile isotropic or anisotropic representative response with their relative density as an input. This relative density may be further optimized by use of the earlier homogenization-based methods proposed by Allaire (1992), allowing for a finite void volume fraction per FVE. Of course, an RSA geometry may also be considered, however, in the context of triangular or trapezoidal FVEs, the circles (and more generally the quadric objects) become highly non-conforming near the

sharp corners of the triangles limiting even further the relative densities that can be reached. In turn, the E-Voronoi have the potential to be implemented in such an assembly process (Martínez et al., 2018) recalling nonetheless the weaker mechanical resilience as compared to the M-Voronoi geometries at finite strains and buckling/fracture loads. One can further envisage a more uniform transition between the FVE boundaries by applying smoothing techniques (Martínez et al., 2016; Kumar et al., 2020). Obviously, the present assembly method is limited by the minimum 3D-printing feature capability, i.e., the minimum void size that can be properly realized in practice.

6. Conclusions

In this study, we propose a versatile mechanically-grown morphogenesis method to obtain high-to-low density isotropic and anisotropic porous and more generally composite materials, called M-Voronoi. The method is based on a combined nonlinear elastic finite strain computational and 3D-printing strategy. In order to achieve sufficient specimen quality, we propose an interruption program during the 3D-printing which consists in alternate additive manufacturing and interruption time increments. The resulting porous specimens are then experimentally tested under uniaxial compression. In particular, the newly proposed M-Voronoi materials exhibit a strong hardening behavior under compressive loads as compared to a number of available voided and cellular materials, which tend to exhibit either a peak stress and a plateau or only weak hardening for most of the deformation process before final densification. This hardening response is mainly a consequence of three geometrical characteristics: (i) the randomness of the void geometries, (ii) the non-uniformity of the intervoid ligaments and (iii) the smooth void geometry reducing efficiently stress localization. In addition, the randomness of the M-Voronoi geometry makes these materials less sensitive to imperfections and realization variations. Nevertheless, a more detailed study is required along this direction perhaps including additional loading conditions such as tensile and hydrostatic ones (Tankasala et al., 2017).

The versatility and generality of the morphogenesis method, which is numerical and is based on solving a nonlinear elastic problem subjected to only Dirichlet boundary conditions, and unlike more classical periodic cells, allows to grow uniformly such M-Voronoi geometries in arbitrary shaped domains or as called in this study, finite volume elements (FVEs), (e.g. triangles, circles, trapezoids, rectangles, etc.). This allows for their easy subsequent assembly into complex macroscopic geometries. A potential implication of such processes is the future use of well-known (Allaire, 1992) as well as more recent (Wang and Sigmund, 2021) optimization techniques to design lightweight structures that behave optimally for a large number of loading states, since the proposed materials can vary from isotropic to anisotropic at different regions in these structures.

On a different note, one could apply more complex non-shape-preserving Dirichlet boundary conditions leading a non-trivial final domain shape. Such a process is beyond the scope of the present study, however, the same design idea presented here is directly applicable to such a case. Note, however, that such non-uniform Dirichlet boundary conditions may lead to boundary inter-penetrations as well as non-uniform inclusion/void concentrations throughout the domain. Yet, it may allow to reach a pre-designed domain shape and thus deserves further study in the future.

Finally, the method proposed here is directly applicable to three-dimensional geometries while any type of composites may be created by simply replacing at the final stage the void phase with any inclusion(s) type that may be required. Such a study is underway. Moreover, a machine learning inverse approach (Kumar et al., 2020) could potentially be extended to the nonlinear response to obtain a targeted family of M-Voronoi materials with "tunable" an-isotropy, since the latter allow for a limitless number of geometries that may be achieved via complex applied mechanical loads. We also note at this point that the void growth mechanism via incompressible nonlinear elasticity may be directly applied to porous solids with or without connectivity and with moderate relative density in order to reach much lower relative densities (such as the spinodal geometries in Portela et al. (2020) and Zerhouni et al. (2021)). Finally, a study of the M-Voronoi geometry using a metallic material is necessary to study the enhancement of the mechanical properties in the latter case. Such an analysis is left for future study.

CRediT authorship contribution statement

Z. Hooshmand-Ahoor: Software, Conceptualization, Methodology, Investigation, Writing – original draft. **M.G. Tarantino:** Methodology, Investigation, Writing – review & editing, Supervision. **K. Danas:** Software, Conceptualization, Methodology, Investigation, Writing – review & editing, Supervision, Funding acquisition.

Declaration of competing interest

The authors declare that they have no known competing financial interests or personal relationships that could have appeared to influence the work reported in this paper.

Data availability

Data will be made available on request.

Acknowledgments

Z.H.A acknowledges support of the Ecole Polytechnique via a Monge scholarship. M.G.T acknowledges partial support from the CNRS Cellule Energie. K.D. acknowledges the partial support from the European Research Council (ERC) under the European Union's Horizon 2020 research and innovation program (grant agreement No 636903 - MAGNETO).

Appendix. Relative density and porosity evolution

We discuss here the evolution of the porous volume fraction or equivalently of the relative density under prescribed uniform displacement (Dirichlet only) boundary conditions. We recall that the solid phase (matrix) is taken to be incompressible, and thus the volume of the cell changes under large deformation, due to void growth only. Therefore, $\mathbf{F}^{\text{app}}$ can be cast in any form (provided of course that $\det \mathbf{F}^{\text{app}} > 0$ to satisfy material impenetrability), although the embedded voids may grow or shrink depending on the magnitude of $\det \mathbf{F}^{\text{app}}$. For the voids to grow one needs $\det \mathbf{F}^{\text{app}} > 1$ and the contrary case to shrink ($0 < \det \mathbf{F}^{\text{app}} < 1$). Denote next the volumes of the matrix and voids in the reference (deformed) configuration to be $\mathcal{V}_0^m$ ($\mathcal{V}^m$) and $\mathcal{V}_0^v$ ($\mathcal{V}^v$), respectively. Then, incompressibility in the matrix phase implies that

$$\mathcal{V}^m = \mathcal{V}_0^m \tag{A.1}$$

while the total volumes in the reference and deformed configurations are given by

$$\mathcal{V}_0 = \mathcal{V}_0^m + \mathcal{V}_0^v, \qquad \mathcal{V} = \mathcal{V}^m + \mathcal{V}^v. \tag{A.2}$$

We note further that the deformed volume of the cell, $\mathcal{V}$, is entirely defined in terms of the applied deformation gradient $\mathbf{F}^{\text{app}}$ by the relation

$$\mathcal{V} = \det \mathbf{F}^{\text{app}}\, \mathcal{V}_0, \tag{A.3}$$

given that $\mathbf{F}^{\text{app}}$ corresponds to the average deformation gradient in the cell (Hill, 1963).

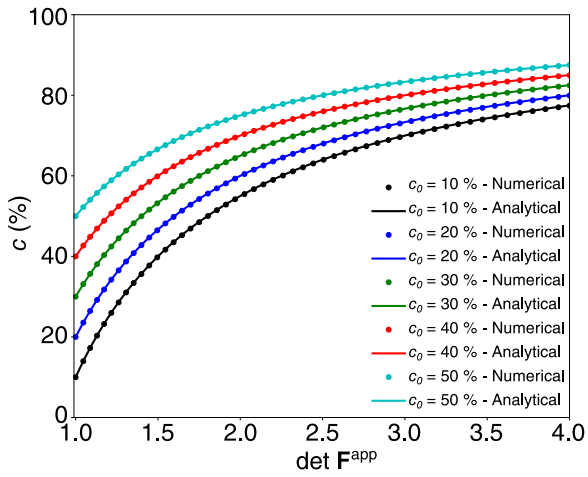

Fig. A.15. Evolution of porosity $c = 1 - \rho$ as a function of the applied determinant of the deformation gradient, as obtained by numerical simulations and the analytical expression (A.9).

Note further that the relative density in the reference, ρ_0 and deformed, ρ, configurations for a porous material are defined as

$$\rho_0 = \frac{\widehat{\rho}_0}{\widehat{\rho}_0^m}, \qquad \rho = \frac{\widehat{\rho}}{\widehat{\rho}^m}. \tag{A.4}$$

Here, $\widehat{\rho}_0^m$ and $\widehat{\rho}^m$ indicate the density of the matrix phase in the reference and deformed configurations, respectively, and $\widehat{\rho}_0$ and $\widehat{\rho}$ the density of the cell in the reference and deformed configurations, respectively.

Moreover, in a porous material, the total mass in the cell, m, is equal to the mass of the matrix, m^m, i.e.,

$$m = \widehat{\rho}_0\, \mathcal{V}_0 = \widehat{\rho}\, \mathcal{V}, \qquad m^m = \widehat{\rho}_0^m\, \mathcal{V}_0^m = \widehat{\rho}^m\, \mathcal{V}^m. \tag{A.5}$$

and thus from mass conservation we have

$$m = m^m \qquad \frac{\widehat{\rho}_0}{\widehat{\rho}_0^m} = \frac{\mathcal{V}_0^m}{\mathcal{V}_0} = \rho_0, \quad \Rightarrow \quad \frac{\widehat{\rho}}{\widehat{\rho}^m} = \frac{\mathcal{V}^m}{\mathcal{V}} = \rho. \tag{A.6}$$

Using the last definitions together with relations (A.1) and (A.3), we readily get

$$\frac{\mathcal{V}^m}{\mathcal{V}} = \frac{1}{\det \mathbf{F}^{\text{app}}} \frac{\mathcal{V}_0^m}{\mathcal{V}_0} \qquad \text{or} \qquad \rho = \frac{\rho_0}{\det \mathbf{F}^{\text{app}}}, \tag{A.7}$$

which corresponds to Eq. (5) in the main text.

One may further define the void volume fraction in the reference, c_0, and deformed configuration, c, as

$$c_0 = \frac{\mathcal{V}_0^v}{\mathcal{V}_0} = \frac{\mathcal{V}_0 - \mathcal{V}_0^m}{\mathcal{V}_0} = 1 - \rho_0, \quad c = \frac{\mathcal{V}^v}{\mathcal{V}} = \frac{\mathcal{V} - \mathcal{V}^m}{\mathcal{V}} = 1 - \rho. \tag{A.8}$$

Using the result (A.7), one readily gets

$$c = 1 - \frac{1 - c_0}{\det \mathbf{F}^{\text{app}}}. \tag{A.9}$$

It can be readily observed that the aforementioned relations are purely kinematic due to the incompressibility of the matrix phase as well as the application of the Dirichlet-only boundary conditions and consequently only $\mathbf{F}^{\text{app}}$ controls the final porosity/relative density of the cell. In the case of mixed Neumann–Dirichlet boundary conditions and incompressible matrix, still the void growth is controlled by the average deformation gradient in the cell but that does not correspond exactly to the partially applied deformation gradient imposed via the displacement field in part of the boundary.

In Fig. A.15, we assess our numerical calculations by simulating RSA voided cells with different initial porosities c_0 applying equi-biaxial loads with $\det \mathbf{F}^{\text{app}} > 1$ and comparing the induced numerical porosity with that obtained by the analytical expression (A.9). In this figure, we observe a nonlinear saturation type increase of the porosity with increasing $\det \mathbf{F}^{\text{app}}$. The numerical simulation recovers to excellent accuracy the exact analytical result (A.9). This saturation type response indicates that very large strains are, in general, necessary to reach very high porosities (or very low relative densities). This, in turn, leads to severe mesh distortion. In order to avoid numerical issues, a strategy consists in ceasing the simulation, extracting the geometry (but not the stress and strain fields), remesh and restart the simulation from the lastly obtained geometry. This allows for an efficient and very accurate resolution at very low relative densities.

Appendix B. Supplementary data

Supplementary material related to this article can be found online at https://doi.org/10.1016/j.mechmat.2022.104432.

References

Aage, N., Andreassen, E., Lazarov, B.S., Sigmund, O., 2017. Giga-voxel computational morphogenesis for structural design. Nature 550 (7674), 84–86. http://dx.doi.org/10.1038/nature23911.

Al-Ketan, O., Lee, D.-W., Al-Rub, R.K.A., 2021. Mechanical properties of additively-manufactured sheet-based gyroidal stochastic cellular materials. Addit. Manuf. 48, 102418. http://dx.doi.org/10.1016/j.addma.2021.102418.

Allaire, G., 1992. Homogenization and two-scale convergence. SIAM J. Math. Anal. 23 (6), 1482–1518. http://dx.doi.org/10.1137/0523084.

Anoukou, K., Brenner, R., Hong, F., Pellerin, M., Danas, K., 2018. Random distribution of polydisperse ellipsoidal inclusions and homogenization estimates for porous elastic materials. Comput. Struct. 210, 87–101. http://dx.doi.org/10.1016/j.compstruc.2018.08.006.

Ashby, M.F., Gibson, L.J., 1997. Cellular solids: structure and properties. Press Syndicate of the University of Cambridge, Cambridge, UK, pp. 175–231. http://dx.doi.org/10.1017/CBO9781139878326.

Baandrup, M., Sigmund, O., Polk, H., Aage, N., 2020. Closing the gap towards super-long suspension bridges using computational morphogenesis. Nature Commun. 11 (1), 1–7. http://dx.doi.org/10.1038/s41467-020-16599-6.

Bi, S., Chen, E., Gaitanaros, S., 2020. Additive manufacturing and characterization of brittle foams. Mech. Mater. 145, 103368. http://dx.doi.org/10.1016/j.mechmat.2020.103368.

Bonatti, C., Mohr, D., 2019. Mechanical performance of additively-manufactured anisotropic and isotropic smooth shell-lattice materials: Simulations & experiments. J. Mech. Phys. Solids 122, 1–26. http://dx.doi.org/10.1016/j.jmps.2018.08.022.

Corson, F., Hamant, O., Bohn, S., Traas, J., Boudaoud, A., Couder, Y., 2009. Turning a plant tissue into a living cell froth through isotropic growth. Proc. Natl. Acad. Sci. 106 (21), 8453–8458. http://dx.doi.org/10.1073/pnas.0812493106.

Crossland, E.J.W., Kamperman, M., Nedelcu, M., Ducati, C., Wiesner, U., Smilgies, D.M., Toombes, G.E.S., Hillmyer, M.A., Ludwigs, S., Steiner, U., Snaith, H.J., 2008. A Bicontinuous Double Gyroid Hybrid Solar Cell 9, 2807–2812, http://dx.doi.org/10.1021/nl803174p.

Deshpande, V., Fleck, N., 2000. Isotropic constitutive models for metallic foams. J. Mech. Phys. Solids 48 (6), 1253–1283. http://dx.doi.org/10.1016/S0022-5096(99)00082-4.

Deshpande, V., Fleck, N., Ashby, M., 2001. Effective properties of the octet-truss lattice material. J. Mech. Phys. Solids 49 (8), 1747–1769. http://dx.doi.org/10.1016/S0022-5096(01)00010-2.

Faisal, T.R., Hristozov, N., Rey, A.D., Western, T.L., Pasini, D., 2012. Experimental determination of Philodendron melinonii and Arabidopsis thaliana tissue microstructure and geometric modeling via finite-edge centroidal Voronoi tessellation. Phys. Rev. E 86 (3), 031921. http://dx.doi.org/10.1103/PhysRevE.86.031921.

Francfort, G., Murat, F., 1986. Homogenization and optimal bounds in linear elasticity. Arch. Ration. Mech. Anal. 94, 307–334. http://dx.doi.org/10.1007/bf00280908.

Gong, L., Kyriakides, S., 2005. Compressive response of open cell foams Part II: Initiation and evolution of crushing. Int. J. Solids Struct. 42 (5–6), 1381–1399. http://dx.doi.org/10.1016/j.ijsolstr.2004.07.024.

Hashin, Z., Shtrikman, S., 1963. A variational approach to the theory of the elastic behaviour of multiphase materials. J. Mech. Phys. Solids 11 (2), 127–140. http://dx.doi.org/10.1016/0022-5096(63)90060-7.

Hill, R., 1963. Elastic properties of reinforced solids: Some theoretical principles. J. Mech. Phys. Solids 11 (5), 357–372. http://dx.doi.org/10.1016/0022-5096(63)90036-X.

Hsieh, M.-T., Endo, B., Zhang, Y., Bauer, J., Valdevit, L., 2019. The mechanical response of cellular materials with spinodal topologies. J. Mech. Phys. Solids 125, 401–419. http://dx.doi.org/10.1016/j.jmps.2019.01.002.

Jang, W.-Y., Kraynik, A.M., Kyriakides, S., 2008. On the microstructure of open-cell foams and its effect on elastic properties. Int. J. Solids Struct. 45 (7–8), 1845–1875. http://dx.doi.org/10.1016/j.ijsolstr.2007.10.008.

Kasza, K., Farrell, D., Zallen, J., 2014. Spatiotemporal control of epithelial remodeling by regulated myosin phosphorylation. PNAS Proc. Nat. Acad. Sci. 111 (32), 11732–11737. http://dx.doi.org/10.1073/pnas.1400520111.

Khristenko, U., Constantinescu, A., Tallec, P.L., Oden, J.T., Wohlmuth, B., 2020. A statistical framework for generating microstructures of two-phase random materials: Application to fatigue analysis. Multiscale Model. Simul. 18 (1), 21–43. http://dx.doi.org/10.1137/19M1259286.

Kumar, S., Tan, S., Zheng, L., Kochmann, D.M., 2020. Inverse-designed spinodoid metamaterials. Npj Comput. Mater. 6 (1), 1–10. http://dx.doi.org/10.1038/s41524-020-0341-6.

Liu, L., Kamm, P., García-Moreno, F., Banhart, J., Pasini, D., 2017. Elastic and failure response of imperfect three-dimensional metallic lattices: the role of geometric defects induced by Selective Laser Melting. J. Mech. Phys. Solids 107, 160–184. http://dx.doi.org/10.1016/j.jmps.2017.07.003.

Liu, Z., Tan, J., Cohen, D., Yang, M., Sniadecki, N., Ruiz, S., Nelson, C., Chen, C., 2010. Mechanical tugging force regulates the size of cell–cell junctions. PNAS Proc. Nat. Acad. Sci. 107 (22), 9944–9949. http://dx.doi.org/10.1073/pnas.0914547107.

Lopez-Pamies, O., Goudarzi, T., Danas, K., 2013. The nonlinear elastic response of suspensions of rigid inclusions in rubber: II—A simple explicit approximation for finite-concentration suspensions. J. Mech. Phys. Solids 61 (1), 19–37. http://dx.doi.org/10.1016/j.jmps.2012.08.013.

Luan, S., Kraynik, A.M., Gaitanaros, S., 2022. Microscopic and macroscopic instabilities in elastomeric foams. Mech. Mater. 164, 104124. http://dx.doi.org/10.1016/j.mechmat.2021.104124.

Ma, J., Zhao, Z.-L., Lin, S., Xie, Y.M., 2021. Topology of leaf veins: Experimental observation and computational morphogenesis. J. Mech. Behav. Biomed. Mater. 123, 104788. http://dx.doi.org/10.1016/j.jmbbm.2021.104788.

Martínez, J., Dumas, J., Lefebvre, S., 2016. Procedural voronoi foams for additive manufacturing. ACM Trans. Graph. 35 (4), 1–12. http://dx.doi.org/10.1145/2897824.2925922.

Martínez, J., Hornus, S., Song, H., Lefebvre, S., 2018. Polyhedral Voronoi diagrams for additive manufacturing. ACM Trans. Graph. 37 (4), 1–15. http://dx.doi.org/10.1145/3197517.3201343.

Maskery, I., Aboulkhair, N., Aremu, A., Tuck, C., Ashcroft, I., 2017. Compressive failure modes and energy absorption in additively manufactured double gyroid lattices. Addit. Manuf. 16, 24–29. http://dx.doi.org/10.1016/j.addma.2017.04.003.

Menges, A., 2012. Biomimetic design processes in architecture: morphogenetic and evolutionary computational design. Bioinspiration Biomim. 7 (1), 015003. http://dx.doi.org/10.1088/1748-3182/7/1/015003.

Michel, J., Lopez-Pamies, O., Ponte Castañeda, P., Triantafyllidis, N., 2007. Microscopic and macroscopic instabilities in finitely strained porous elastomers. J. Mech. Phys. Solids 55 (5), 900–938. http://dx.doi.org/10.1016/j.jmps.2006.11.006.

Ohno, N., Okumura, D., Noguchi, H., 2002. Microscopic symmetric bifurcation condition of cellular solids based on a homogenization theory of finite deformation. J. Mech. Phys. Solids 50 (5), 1125–1153. http://dx.doi.org/10.1016/S0022-5096(01)00106-5.

O'Masta, M.R., Dong, L., St-Pierre, L., Wadley, H., Deshpande, V.S., 2017. The fracture toughness of octet-truss lattices. J. Mech. Phys. Solids 98, 271–289. http://dx.doi.org/10.1016/j.jmps.2016.09.009.

Onck, P., Andrews, E., Gibson, L., 2001. Size effects in ductile cellular solids. Part I: modeling. Int. J. Mech. Sci. 43 (3), 681–699. http://dx.doi.org/10.1016/S0020-7403(00)00042-4.

Papka, S.D., Kyriakides, S., 1994. In-plane compressive response and crushing of honeycomb. J. Mech. Phys. Solids 42 (10), 1499–1532. http://dx.doi.org/10.1016/0022-5096(94)90085-X.

Papka, S., Kyriakides, S., 1998. Experiments and full-scale numerical simulations of in-plane crushing of a honeycomb. Acta Mater. 46 (8), 2765–2776. http://dx.doi.org/10.1016/S1359-6454(97)00453-9.

Portela, C.M., Vidyasagar, A., Krödel, S., Weissenbach, T., Yee, D.W., Greer, J.R., Kochmann, D.M., 2020. Extreme mechanical resilience of self-assembled nanolabyrinthine materials. Proc. Natl. Acad. Sci. 117 (11), 5686–5693. http://dx.doi.org/10.1073/pnas.1916817117.

Prusty, R., Narayan, R., Scherer, M., Steiner, U., Deshpande, V., Fleck, N., Ramamurty, U., 2020. Spherical indentation response of a Ni double gyroid nanolattice. Scr. Mater. 188, 64–68. http://dx.doi.org/10.1016/j.scriptamat.2020.07.011.

Roberts, A., Garboczi, E., 2001. Elastic moduli of model random three-dimensional closed-cell cellular solids. Acta Mater. 49 (2), 189–197. http://dx.doi.org/10.1016/S1359-6454(00)00314-1.

Roberts, A.P., Teubner, M., 1995. Transport properties of heterogeneous materials derived from Gaussian random fields: Bounds and simulation. Phys. Rev. E 51 (5), 4141–4154. http://dx.doi.org/10.1103/PhysRevE.51.4141.

Roudavski, S., 2009. Towards morphogenesis in architecture. Int. J. Archit. Comput. 7 (3), 345–374. http://dx.doi.org/10.1260/147807709789621266.

San Marchi, C., Mortensen, A., 2001. Deformation of open-cell aluminum foam. Acta Mater. 49 (19), 3959–3969. http://dx.doi.org/10.1016/S1359-6454(01)00294-4.

Schaedler, T.A., Carter, W.B., 2016. Architected cellular materials. Annu. Rev. Mater. Res. 46, 187–210. http://dx.doi.org/10.1146/annurev-matsci-070115-031624.

Segurado, J., Llorca, J., 2002. A numerical approximation to the elastic properties of sphere-reinforced composites. J. Mech. Phys. Solids 50, http://dx.doi.org/10.1016/S0022-5096(02)00021-2.

Spyrou, L., Brisard, S., Danas, K., 2019. Multiscale modeling of skeletal muscle tissues based on analytical and numerical homogenization. J. Mech. Behav. Biomed. Mater. 92, 97–117. http://dx.doi.org/10.1016/j.jmbbm.2018.12.030.

Symons, D.D., Fleck, N.A., 2008. The imperfection sensitivity of isotropic two-dimensional elastic lattices. J. Appl. Mech. 75 (5), http://dx.doi.org/10.1115/1.2913044.

Tancogne-Dejean, T., Diamantopoulou, M., Gorji, M.B., Bonatti, C., Mohr, D., 2018. 3D plate-lattices: An emerging class of low-density metamaterial exhibiting optimal isotropic stiffness. Adv. Mater. 30 (45), 1803334. http://dx.doi.org/10.1002/adma.201803334.

Tankasala, H., Deshpande, V., Fleck, N., 2017. Tensile response of elastoplastic lattices at finite strain. J. Mech. Phys. Solids 109, 307–330. http://dx.doi.org/10.1016/j.jmps.2017.02.002.

Tarantino, M.-G., Danas, K., 2019. Programmable higher-order Euler buckling modes in hierarchical beams. Int. J. Solids Struct. 167, 170–183. http://dx.doi.org/10.1016/j.ijsolstr.2019.03.009.

Tarantino, M.-G., Zerhouni, O., Danas, K., 2019. Random 3D-printed isotropic composites with high volume fraction of pore-like polydisperse inclusions and near-optimal elastic stiffness. Acta Mater. 175, 331–340. http://dx.doi.org/10.1016/j.actamat.2019.06.020.

Tekoglu, C., Gibson, L., Pardoen, T., Onck, P., et al., 2011. Size effects in foams: Experiments and modeling. Prog. Mater. Sci. 56 (2), 109–138. http://dx.doi.org/10.1016/j.pmatsci.2010.06.001.

Teubner, M., 1991. Level surfaces of Gaussian random fields and microemulsions. Europhys. Lett. (EPL) 14 (5), 403–408. http://dx.doi.org/10.1209/0295-5075/14/5/003.

Thornton, P., Magee, C., 1975. Deformation characteristics of zinc foam. Metall. Trans. A 6 (9), 1801–1807. http://dx.doi.org/10.1007/BF02642310.

Tidball, J.G., Wehling-Henricks, M., 2004. Evolving therapeutic strategies for Duchenne muscular dystrophy: targeting downstream events. Pediatr. Res. 56 (6), 831–841. http://dx.doi.org/10.1203/01.PDR.0000145578.01985.D0.

Torquato, S., 1997. Effective stiffness tensor of composite media—I. Exact series expansions. J. Mech. Phys. Solids 45 (9), 1421–1448. http://dx.doi.org/10.1016/S0022-5096(97)00019-7.

Torquato, S., 2002. Random Heterogeneous Materials: Microstructure and Macroscopic Properties. Springer, New York, http://dx.doi.org/10.1115/1.1483342.

Triantafillou, T., Gibson, L., 1990. Multiaxial failure criteria for brittle foams. Int. J. Mech. Sci. 32 (6), 479–496. http://dx.doi.org/10.1016/0020-7403(90)90154-B.

Triantafyllidis, N., Schraad, M., 1998. Onset of failure in aluminum honeycombs under general in-plane loading. J. Mech. Phys. Solids 46 (6), 1089–1124. http://dx.doi.org/10.1016/S0022-5096(97)00060-4.

van Nuland, T., van Dommelen, J., Geers, M., 2021. An anisotropic Voronoi algorithm for generating polycrystalline microstructures with preferred growth directions. Comput. Mater. Sci. 186, 109947. http://dx.doi.org/10.1016/j.commatsci.2020.109947.

Wang, F., Sigmund, O., 2021. 3D architected isotropic materials with tunable stiffness and buckling strength. J. Mech. Phys. Solids 152, 104415. http://dx.doi.org/10.1016/j.jmps.2021.104415.

Wu, J., Aage, N., Westermann, R., Sigmund, O., 2017. Infill optimization for additive manufacturing—approaching bone-like porous structures. IEEE Trans. Vis. Comput. Graphics 24 (2), 1127–1140. http://dx.doi.org/10.1109/TVCG.2017.2655523.

Zerhouni, O., Brisard, S., Danas, K., 2021. Quantifying the effect of two-point correlations on the effective elasticity of specific classes of random porous materials with and without connectivity. Internat. J. Engrg. Sci. 166, 103520. http://dx.doi.org/10.1016/j.ijengsci.2021.103520.

Zerhouni, O., Tarantino, M.-G., Danas, K., 2019. Numerically-aided 3D printed random isotropic porous materials approaching the Hashin-Shtrikman bounds. Composites B 156, 344–354. http://dx.doi.org/10.1016/j.compositesb.2018.08.032.

Zerhouni, O., Tarantino, M.-G., Danas, K., Hong, F., 2018. Influence of the internal geometry on the elastic properties of materials using 3D printing of computer-generated random microstructures. In: 2018 SEG International Exposition and Annual Meeting. OnePetro, http://dx.doi.org/10.1190/segam2018-2998182.1.

Zhao, Z.-L., Zhou, S., Feng, X.-Q., Xie, Y.M., 2018. On the internal architecture of emergent plants. J. Mech. Phys. Solids 119, 224–239. http://dx.doi.org/10.1016/j.jmps.2018.06.014.